

See discussions, stats, and author profiles for this publication at: <https://www.researchgate.net/publication/322093936>

Bi-directional vibration control of offshore wind turbines using a 3D pendulum tuned mass damper

Article in Mechanical Systems and Signal Processing · May 2018

DOI: 10.1016/j.ymssp.2017.12.011

CITATIONS

18

READS

868

2 authors:



Chao Sun

Louisiana State University

27 PUBLICATIONS 268 CITATIONS

[SEE PROFILE](#)



Vahid Jahangiri

Louisiana State University

10 PUBLICATIONS 64 CITATIONS

[SEE PROFILE](#)

Some of the authors of this publication are also working on these related projects:



Vibration Control of Monopile Offshore Wind Turbine [View project](#)



Concrete Constitutive Law Modeling Using CT Technique [View project](#)



Bi-directional vibration control of offshore wind turbines using a 3D pendulum tuned mass damper

C. Sun*, V. Jahangiri

Department of Civil and Environmental Engineering, Louisiana State University, Baton Rouge, LA 70803, USA

ARTICLE INFO

Article history:

Received 19 September 2017

Received in revised form 1 December 2017

Accepted 9 December 2017

Keywords:

Offshore wind turbines

Bi-directional vibration control

Wind-wave misalignment

Pendulum tuned mass damper

ABSTRACT

Offshore wind turbines suffer from excessive bi-directional vibrations due to wind-wave misalignment and vortex induced vibrations. However, most of existing research focus on unidirectional vibration attenuation which is inadequate for real applications. The present paper proposes a three dimensional pendulum tuned mass damper (3d-PTMD) to mitigate the tower and nacelle dynamic response in the fore-aft and side-side directions. An analytical model of the wind turbine coupled with the 3d-PTMD is established wherein the interaction between the blades, the tower and the 3d-PTMD is modeled. Aerodynamic loading is computed using the Blade Element Momentum method where the Prandtl's tip loss factor and the Glauert correction are considered. JONSWAP spectrum is adopted to generate wave data. Wave loading is computed using Morison's equation in collaboration with the strip theory. Via a numerical search approach, the design formula of the 3d-PTMD is obtained and examined on a National Renewable Energy Lab (NREL) monopile 5 MW baseline wind turbine model under misaligned wind, wave and seismic loading. Dual linear tuned mass dampers (TMDs) deployed in the fore-aft and side-side directions are utilized for comparison. It is found that the 3d-PTMD with a mass ratio of 2% can improve the mitigation of the root mean square and peak response by around 10% when compared with the dual linear TMDs in controlling the bi-directional vibration of the offshore wind turbines under misaligned wind, wave and seismic loading.

© 2017 Elsevier Ltd. All rights reserved.

1. Introduction

Because of advantages such as higher wind speed, less visual impacts and less noise constraints in the marine area, offshore wind plants are becoming increasingly attractive for wind energy production. However, the combined wind-wave loading and other environmental effects will render the offshore wind turbines (OWTs) suffering from excessive vibration, adversely influencing the system performance and the structural integrity. In this regard, structural vibration control, which has been successfully employed in civil structures, is being studied in recent years to mitigate the vibration of OWTs.

Three basic control strategies have been developed: passive, semi-active and active [1,2]. Passive control of offshore wind turbines has been studied actively in the passed decade. Murtagh et al. [3] studied the control of the wind turbine along-wind vibration using a passive tuned mass damper (TMD). Colwell et al. [4] used the tuned liquid column damper to control the vibration of an offshore wind turbine. Research findings indicated that the tuned liquid column dampers could increase the tower fatigue life. Lackner et al. [5] used dual linear passive TMDs placed in the nacelle to control the fore-aft and

* Corresponding author.

E-mail address: csun@lsu.edu (C. Sun).

In comparison, semi-active control devices are more applicable to systems with time-variant parameters. Semi-active TMDs (STMDs) have been investigated and demonstrated effective in controlling vibration of linear and nonlinear systems subjected to stationary and non-stationary excitations [6, 7, 8]. Weber [9] utilized a semi-active vibration absorber with real-time adjusted magnetorheological damper (MR-SVA) to mitigate harmonic loading induced vibrations. It was found that the MR-SVA outperforms the passive TMD. Huang and Arrigan *et al.* [10, 11] explored the mitigation of wind turbine blades using the STMDs retuned in real-time via a short time Fourier transform (STFT) based control algorithm. The authors found that the STMDs could mitigate the blade responses under varying operational or environmental conditions. Sun *et al.* [12] further advanced the control algorithm used in Ref. [6, 10, 11] by incorporating the tuning of damping ratio. The authors examined the performance of the modified control algorithm for seismic protection and observed improved mitigation effect. Recently, Sun [13] studied the mitigation of offshore wind turbines under multiple hazards consisting of wind, wave and seismic loading using the STMD. It was found that the STMD outperforms the passive TMD in mitigating the structural response under the combined effects of multiple hazards, soil effects and structural damage.

Active control of vibrations have been studied and demonstrated effective under operational or environmental variations [14, 15]. Staino *et al.* [16] used active tendons mounted inside the blade to control the edgewise vibration of wind turbine blades. The authors concluded that the proposed control scheme can significantly mitigate the response of the blade. Fitzgerald *et al.* [17] utilized an active tuned mass damper to control the in-plane vibration of the blades. It was found that the active TMDs can provide better reduction than the passive TMDs.

However, most of the aforementioned literatures focus on one-directional response (fore-aft motion) mitigation while the real OWTs suffer from bi-directional vibration (fore-aft and side-side) due to wind-wave misalignment, vortex induced cross-wind vibration and other misaligned loading such as earthquakes. Perhaps the dual TMDs used in Refs. [5] could mitigate the vibration in the fore-aft and side-side directions, there are still several limitations existing in this approach. First, the optimal mass allocation (given total TMD mass) and the optimal arrangement (relative angle between the two TMDs) are correlated with the probabilistic distribution of the magnitude and directionality of the external loading and thus can always be a challenge for the design. It is probable that the utilization efficiency of the two TMDs can be relatively low. For instance, the TMD in the fore-aft direction is fully involved while the one in the side-side direction is almost at rest when only the fore-aft vibration is induced, and vice versa. In addition, the dual TMDs require more space, larger mass and more cost for the installation and maintenance.

Due to the simplicity of installation and maintenance, pendulum tuned mass dampers (PTMDs) have been investigated and widely applied in high-rise slender buildings. The natural frequency of the pendulum is tunable through varying the pendulum length. Gerges *et al.* [18] determined the optimum design formula for planar PTMDs under wind and earthquake excitations represented by white noise. To account for the space motion of the PTMDs, Roffel *et al.* [19] proposed the optimum design formula for the PTMD aiming to minimize the acceleration root mean square (RMS) of slender tall buildings under wind loading. It was shown that the optimum design parameters in Ref.[19] were obviously different from the optimum design proposed in Ref.[18]. The difference is partly due to the fact that the optimum objective in [18] is to minimize the displacement RMS while the optimum objective in [19] is to minimize the acceleration RMS. Recently, Sun *et al.* [8, 21] investigated planar adaptive PTMDs (APTMDs) whose natural frequency and damping properties can be retuned in real-time to account for structural or environmental variations. The authors found that the APTMDs could effectively reduce the vibration and prevent the occurrence of bifurcation in nonlinear systems.

To address the limitations of the dual TMDs approach, the present paper proposes a three dimensional pendulum tuned mass damper (3d-PTMD) to control the bi-directional vibration of the monopile OWTs. Since the wind turbine tower is axial-symmetric, the natural frequencies of the fore-aft and side-side directions are almost identical. This renders the 3d-PTMDs suitable for wind turbine bi-directional vibration mitigation. Novelty of the present study is twofold. First, on the basis of the author's previous work[13], a nonlinear mathematical model of the monopile offshore wind turbines coupled with the 3d-PTMD will be established. Aerodynamic loading, wave loading, seismic loading and gravity loading are incorporated in

the model. Second, the optimal design parameters to minimize the nacelle displacement RMS will be determined using a numerical search approach. On the basis of this, the effectiveness of the proposed 3d-PTMD in controlling the bi-directional vibration will be evaluated under misaligned wave-wave and seismic loading. The dual TMDs designed based on [22] are used for comparison. It is found that the 3d-PTMD outperforms the dual linear TMDs in controlling the bi-directional vibration caused by misaligned loading. Furthermore, the proposed 3d-PTMD experience a much smaller stroke than the dual TMDs, which is of significant value for practical application.

2. Establishment of the Analytical Model

A fully coupled three dimensional dynamic model with and without the 3d-PTMD is established using the Euler-Lagrangian equation. The model contains 12 degree-of-freedom (DOF) for the uncontrolled system and 14 DOF for the controlled system.

2.1. Model Description

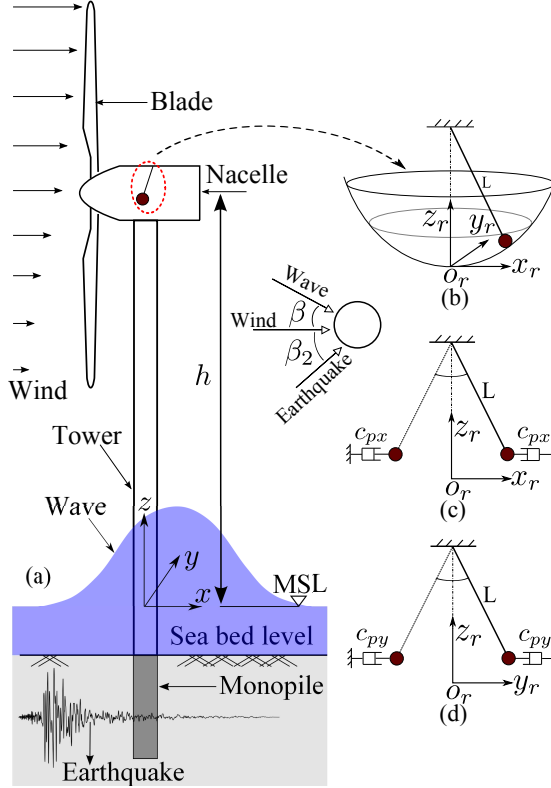


Figure 1: Monopile offshore wind turbine coupled with a three dimensional pendulum tuned mass damper under wind, wave and seismic loading. (a): original schematic model; (b): configuration of the pendulum damper; (c): pendulum model in xz plane; (d): pendulum model in yz plane.

A general monopile offshore wind turbine model subjected to the combination of wind, wave and seismic loading is illustrated in Fig. 1. As shown in Fig. 1, the global coordinate system originates at the intersection of the tower center line and the mean sea level (MSL). In Fig. 1(a), the PTMD is installed in the nacelle. The wind-wave misalignment is denoted by β and wind, earthquake misalignment is denoted by β_2 . When the nacelle translates in two horizontal directions, the pendulum will move along the spherical surface as portrayed in Fig. 1(b). A local coordinate system $x_r y_r z_r - o_r$ is established originating at the rest position

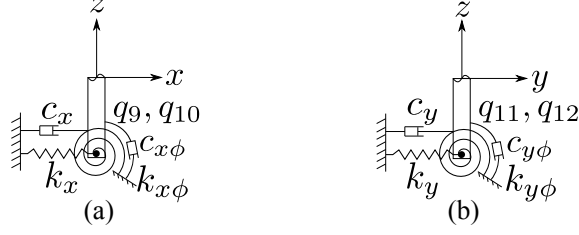


Figure 2: Simplified found model of the offshore wind turbine; (a) foundation model in xz plane; (a) foundation model in yz plane.

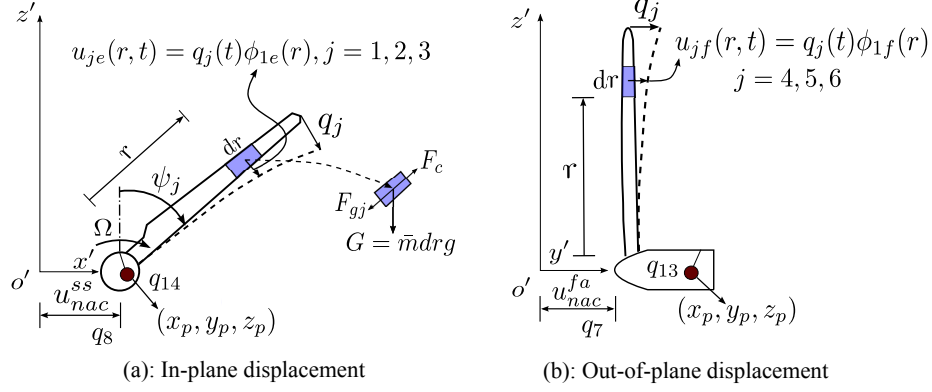


Figure 3: Coordinates of the turbine blades and the nacelle. (a): edgewise vibration; (b): flapwise vibration.

of the pendulum. Fig. 1(c) shows the pendulum motion in the fore-aft direction where c_{px} is the damping coefficient of the damper in x_r direction. Fig. 1(d) shows the pendulum motion in the side-side direction where c_{py} is the damping coefficient of the damper in y_r direction.

Simplified foundation models in the xz and yz planes are shown in Fig. 2 (a) and (b). Soil effects are considered and represented by translational springs with coefficients of k_x , k_y and rotational springs with coefficients of $k_{x\phi}$ and $k_{y\phi}$. The damping property of the soil are considered by introducing translational and rotational dash-pot dampers with coefficients of c_x , c_y , $c_{x\phi}$ and $c_{y\phi}$. Parameters q_9 , q_{10} , q_{11} and q_{12} denote the translation and rotation coordinates of the foundation.

Fig. 3 illustrates the coordinates of the blades(edgewise and flapwise), the nacelle and the PTMD. In Fig. 3, parameters $q_1 \sim q_3$ denote the edgewise coordinates of the three blades and $q_4 \sim q_6$ denote the flapwise coordinates. Parameters q_7 and q_8 denote the relative coordinates of the nacelle in the fore-aft and side-side directions with respect to the foundation. Parameters q_{13} , q_{14} denote the relative coordinate of the PTMD with respect to the nacelle. The blades rotating speed is Ω and the azimuthal angle $\psi_j(t)$ of the j^{th} blade can be expressed as:

$$\psi_j = \Omega t + \frac{2\pi}{3}(j - 1), \quad j = 1, 2, 3 \quad (1)$$

2.2. Euler-Lagrangian Equation

The Euler-Lagrangian equation is used to derive the mathematical model of the monopile offshore wind turbine with the 3d-PTMD. The equation is listed as follows:

$$\frac{d}{dt} \frac{\partial T(t, \tilde{q}(t), \dot{\tilde{q}}(t))}{\partial \dot{q}_i(t)} - \frac{\partial T(t, \tilde{q}(t), \dot{\tilde{q}}(t))}{\partial q_i(t)} + \frac{\partial V(t, \tilde{q}(t))}{\partial q_i(t)} = Q_i(t) \quad (2)$$

where T and V are the system kinetic and potential energy, $\tilde{q}(t)$ is the generalized coordinates vector,

$Q_i(t)$ is the generalized force corresponding to the i^{th} component of $\tilde{q}(t)$. Sign $\dot{(\)}$ denotes the first derivative with respect to time.

2.3. Kinetic Energy

Let parameters q_7 and q_8 denote the relative coordinates of the nacelle in the fore-aft and side-side directions with respect to the foundation. In terms of Fig. 1 and Fig. 3, the absolute displacement of the nacelle in the fore-aft direction u_{nac}^{fa} and the side-side direction u_{nac}^{ss} can be expressed as:

$$\begin{aligned} u_{nac}^{fa} &= q_7 + q_9 + h \tan(q_{10}) \approx q_7 + q_9 + h q_{10} \\ u_{nac}^{ss} &= q_8 + q_{11} + h \tan(q_{12}) \approx q_8 + q_{11} + h q_{12} \end{aligned} \quad (3)$$

where h is the nacelle height with reference to the sea bed.

The absolute velocity of the nacelle in the fore-aft direction v_{nac}^{fa} and the side-side direction v_{nac}^{ss} can be expressed as:

$$\begin{aligned} v_{nac}^{fa} &= \dot{q}_7 + \dot{q}_9 + h \dot{q}_{10} \\ v_{nac}^{ss} &= \dot{q}_8 + \dot{q}_{11} + h \dot{q}_{12} \end{aligned} \quad (4)$$

The resultant absolute velocity of the nacelle v_{nac} can be written as:

$$v_{nac} = \sqrt{(v_{nac}^{fa})^2 + (v_{nac}^{ss})^2} \quad (5)$$

To represent the motion of the blade, a local coordinate system $x'y'z' - o'$ originating at the center of the hub front surface(static state) is established as shown in Fig. 3 where the nacelle has a side-side displacement u_{nac}^{ss} and a fore-aft displacement u_{nac}^{fa} . Displacement of the j^{th} blade is illustrated in Fig. 3. Variables $u_{je}(r, t)$ and $u_{jf}(r, t)$ represent the edgewise and flapwise displacements of the point at a distance r from the blade root; variables ϕ_{1e} and ϕ_{1f} denote the edgewise and flapwise fundamental mode shape. The motion of the nacelle in z direction is minimal and ignored.

Consider an infinitesimal unit dr of the j^{th} blade in Fig. 3, the coordinate of the unit in the $x'y'z' - o'$ system can be represented as:

$$\begin{aligned} x'_r &= u_{nac}^{ss} + r \sin \psi_j + u_{je} \cos \psi_j \\ y'_r &= u_{nac}^{fa} + u_{jf} \\ z'_r &= r \cos \psi_j - u_{je} \sin \psi_j \end{aligned} \quad (6)$$

Taking the first derivative of the coordinates gives the velocity component as:

$$\begin{aligned} \dot{x}'_r &= v_{nac}^{ss} + \Omega r \cos \psi_j + \dot{q}_j \phi_{1e} \cos \psi_j - \Omega q_j \phi_{1e} \sin \psi_j \\ \dot{y}'_r &= v_{nac}^{fa} + \dot{q}_{j+3} \phi_{1f} \\ \dot{z}'_r &= -\Omega r \sin \psi_j - \dot{q}_j \phi_{1e} \sin \psi_j - \Omega q_j \phi_{1e} \cos \psi_j \end{aligned} \quad (7)$$

The absolute velocity magnitude of the unit dr is:

$$v_{bj}(r, t) = \sqrt{\dot{x}'_r{}^2 + \dot{y}'_r{}^2 + \dot{z}'_r{}^2} \quad (8)$$

The absolute velocity $v_{tow}(z, t)$ of an infinitesimal unit dz of the tower can be expressed as:

$$v_{tow} = \sqrt{[\dot{q}_8\phi_{1t} + \dot{q}_{11} + z\dot{q}_{12}]^2 + [\dot{q}_7\phi_{1t} + \dot{q}_9 + z\dot{q}_{10}]^2} \quad (9)$$

In terms of Fig. 1, the absolute coordinate of the pendulum can be formulated as:

$$\begin{aligned} x_p &= u_{nac}^{ss} + x_r \\ y_p &= u_{nac}^{fa} + y_r \\ z_p &= L - \sqrt{L^2 - x_r^2 - y_r^2} \end{aligned} \quad (10)$$

The kinetic energy of the pendulum T_p is:

$$\begin{aligned} T_p &= \frac{1}{2}m_p(\dot{x}_p^2 + \dot{y}_p^2 + \dot{z}_p^2) \\ &= \frac{m_p}{2} \left[(v_{nac}^{ss})^2 + (v_{nac}^{fa})^2 + 2v_{nac}^{ss}\dot{x}_r + 2v_{nac}^{fa}\dot{y}_r + \dot{x}_r^2 + \dot{y}_r^2 + \frac{\sqrt{L^2 - x_r^2 - y_r^2}}{(v_{nac}^{ss}\dot{x}_r + v_{nac}^{fa}\dot{y}_r)^2} \right] \end{aligned} \quad (11)$$

where m_p denotes the mass of the 3d-PTMD.

Therefore, the kinetic energy of the controlled wind turbine system can be expressed as:

$$T = \frac{1}{2} \sum_{j=1}^3 \int_0^R \bar{m} v_{bj}^2(r, t) dr + \frac{1}{2} M_{nac} v_{nac}^2 + \frac{1}{2} \int_0^h \bar{M} v_{tow}^2 dz + \frac{1}{2} M_f [\dot{q}_9^2(t) + \dot{q}_{11}^2(t)] + \frac{1}{2} I_f [\dot{q}_{10}^2(t) + \dot{q}_{12}^2(t)] + T_p \quad (12)$$

where M_{nac} is the mass of the nacelle(including the hub mass); M_f and I_f denote the mass and moment of inertial of the foundation; \bar{m} and \bar{M} denote the mass density per length of the blade and the tower.

2.4. Potential Energy

The total potential energy of the blades is calculated considering the strain energy of the blades due to bending, the centrifugal stiffening effect and the gravity related potential energy.

In terms of Ref. [13], the total potential energy of the blades can be represented as:

$$V_b = \frac{1}{2} \sum_{j=1}^3 [(k_{eg} + k_{ge, eg} - k_{gr, eg} \cos \psi_j) q_j^2 + (k_{fp} + k_{ge, fp} - k_{gr, fp} \cos \psi_j) q_{j+3}^2] \quad (13)$$

where

$$\begin{aligned} k_{eg} &= \int_0^R EI_{eg}(r) (\phi_{1e}'')^2 dr, \quad k_{fp} = \int_0^R EI_{fp}(r) (\phi_{1f}'')^2 dr, \\ k_{ge, eg} &= \Omega^2 \int_0^R \int_r^R [\bar{m}(\xi) \xi d\xi] (\phi_{1e}')^2 dr, \quad k_{ge, fp} = \Omega^2 \int_0^R \int_r^R [\bar{m}(\xi) \xi d\xi] (\phi_{1f}')^2 dr \\ k_{gr, eg} &= g \int_0^R \int_r^R [\bar{m}(\xi) d\xi] (\phi_{1e}')^2 dr, \quad k_{gr, fp} = g \int_0^R \int_r^R [\bar{m}(\xi) d\xi] (\phi_{1f}')^2 dr \end{aligned} \quad (14)$$

I_{eg} and I_{fp} are the moment of inertia in the edgewise and flapwise direction, Ω is the turbine rotating speed, g is the acceleration due to gravity. Sign $()'$ and $()''$ denote the first and second derivatives with respect to length r .

Taking the static position of the pendulum (x_r y_r plane) as the reference, potential energy of the pendulum V_p is:

$$V_p = m_p g (L - \sqrt{L^2 - x_r^2 - y_r^2}) \quad (15)$$

Hence, the total potential energy V of the wind turbine system is:

$$V = V_b + \frac{1}{2}k_t^{fa}q_7^2(t) + \frac{1}{2}k_t^{ss}q_8^2(t) + \frac{1}{2}k_xq_9^2(t) + \frac{1}{2}k_yq_{11}^2(t) + \frac{1}{2}k_{x\phi}q_{10}^2(t) + \frac{1}{2}k_{y\phi}q_{12}^2(t) + V_p \quad (16)$$

where k_t^{fa} and k_t^{ss} denote the fore-aft and side-side stiffness of the tower.

2.5. System Equation of Motion

Substituting Eq. (12) and Eq. (16) into Eq. (2) yields the equations of motion, which can be written in a matrix form as:

$$\tilde{M}\ddot{\tilde{q}} + \tilde{C}\dot{\tilde{q}} + \tilde{K}\tilde{q} = \tilde{Q}_{wind} + \tilde{Q}_{wv} + \tilde{Q}_{seismic} + \tilde{F} \quad (17)$$

where \tilde{M}, \tilde{C} and \tilde{K} are the system mass, damping and stiffness matrices.

Two sets of system matrices for the uncontrolled and controlled systems have been derived and are listed in the Appendix. Variables \tilde{Q}_{wind} , \tilde{Q}_{wv} and $\tilde{Q}_{seismic}$ are the generalized force vectors corresponding to wind, wave and seismic loading, which are derived in the following section. It is noted that Eq.(17) is essentially nonlinear since \tilde{M} , \tilde{C} and \tilde{K} are time-variant. Variable \tilde{F} as shown in Eq. (55) in Appendix B is the generalized force caused by the nonlinearity of the pendulum.

3. Loading

This section presents the derivation of wind, wave and seismic loadings based on the Principle of Virtual Work.

3.1. Wind Turbulence Model

Wind velocity can be represented by a constant mean velocity and a turbulent component, i.e. $v(t) = \bar{v} + \tilde{v}(t)$. In the present study, the logarithmic wind profile is adopted to calculate the mean velocity $\bar{v}(z)$, i.e.

$$\bar{v}(z) = V_{ref} \frac{\log(z/z_0)}{\log(H_{ref}/z_0)} \quad (18)$$

where V_{ref} is the mean velocity at the reference height $H_{ref} = 90m$. Parameter z_0 is the length of roughness and its value is $z_0 = 0.03$.

The turbulent component of wind velocity $\tilde{v}(t)$ is computed using the IEC Kaimal spectral model which is described by the following equations:

$$S_v(f) = \frac{4I^2L_c}{(1 + 6fL_c/\bar{v})^{5/3}} \quad (19)$$

where $S_v(f)$ is the power spectral density function, f is the wind frequency in Hz , I is the wind turbulence intensity and L_c is an integral scale parameter.

To account for the spatial dependency of wind velocity $\tilde{v}(z, t)$ at different points, the cross spectra between two points i and j are defined as:

$$S_{ij}(f) = Coh(i, j; f) \sqrt{S_{ii}(f)S_{jj}(f)} \quad (20)$$

where S_{ij} is the cross spectra, S_{ii} and S_{jj} are the auto spectra at points i and j , respectively.

Referring to the IEC spectral mode[20], the spatial coherence function is given as:

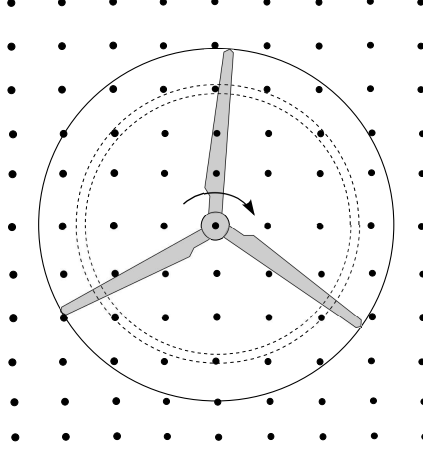


Figure 4: Illustration of the 3D wind field profile covering the rotor disk.

$$Coh(i, j; f) = \exp \left(-a \sqrt{\left(\frac{fL}{\bar{v}_{hub}} \right)^2 + \left(\frac{0.12L}{L_c} \right)^2} \right) \quad (21)$$

where L is the distance between points i and j on the grid, a is the coherence decrement, and L_c is a coherence scale parameter, \bar{v}_{hub} is the mean hub-height wind speed.

In terms of IEC-64000-1 3rd, $a = 12$ and $L_c = 340.2m$ are adopted in the present study.

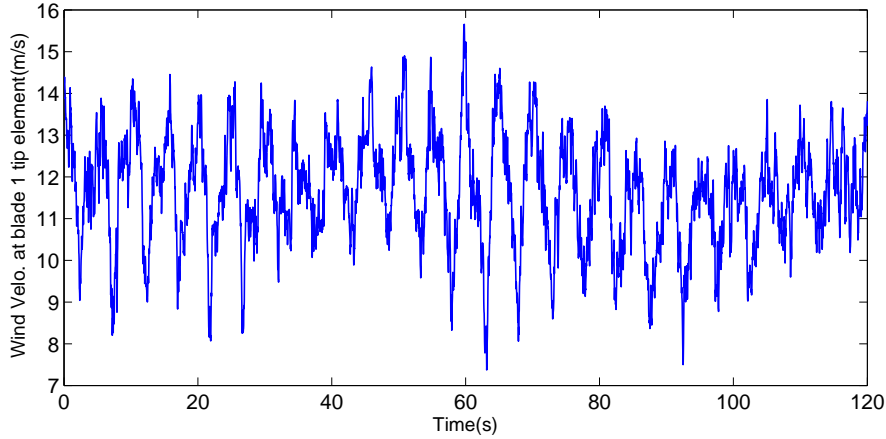


Figure 5: Wind velocity at the tip element of blade 1. ($\bar{v} = 12m/s$ at hub height and turbulence intensity $TI = 10\%$)

Based on Eqns. (18~21), a three dimensional wind field profile covering the domain of the rotor disk is generated using the TurbSim program [20]. A 31×31 velocity grids, as conceptually illustrated in Fig. 4 is produced to represent the three dimensional wind field. Matlab code has been developed to map the full wind field profile onto each span station of the rotating blades. As an illustration, the wind velocity time history at the center of the tip element of blade 1 is shown in Fig. 5 where $\bar{v} = 12m/s$ and the turbulence intensity is $TI = 10\%$.

3.2. Aerodynamic Loading

In the present study, the Blade Element Momentum (BEM) theory is used to estimate the aerodynamic loading acting on the rotating blades. The BEM method is a combination of the momentum theory and

the blade element theory. Time series of the aerodynamic loading are computed based on the momentum theory, the blade characteristics and the operational conditions. The input parameters include the rotor geometry (number of blades, twist, chord distribution, and the airfoils), wind speed and the blade rotational velocity[23].

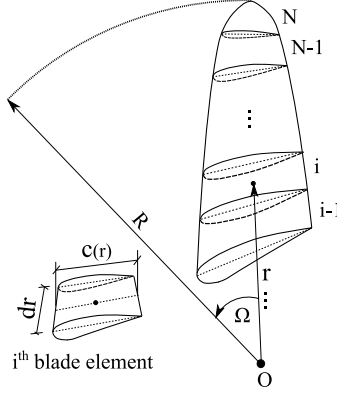


Figure 6: Turbine blade discretized into N blade elements for BEM analysis.

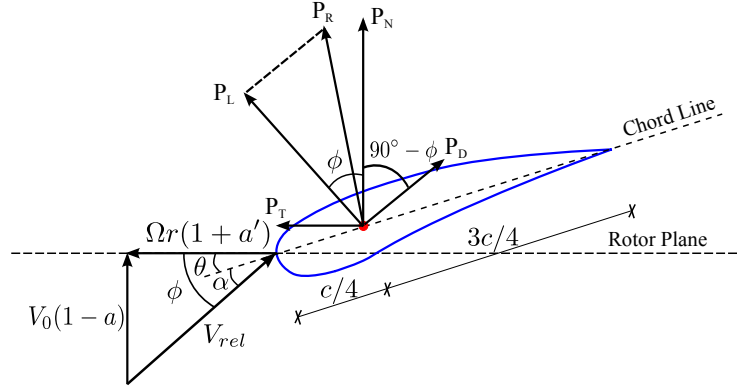


Figure 7: Blade element section subjected to local velocity and aerodynamic loading.

Fig. 6 illustrates a general turbine blade discretized into N elements for BEM analysis where R is the rotor radius and Ω is the rotation velocity. It is assumed in the BEM theory that no radial dependency exists along the blade span and thus the elements can be analyzed independently via performing the momentum theory. In Fig. 6, the i^{th} blade element at a distance r is detailed where dr is the element span length and $c(r)$ is the chord length at the element mid-span.

An arbitrary blade element experiencing local velocities and aerodynamic loading is illustrated in Fig. 7. The relative wind velocity V_{rel} with reference to the the element shown in Fig. 7 can be expressed by combining the axial velocity $v(1-a)$ and the tangential velocity $\Omega r(1+a')$ as:

$$V_{rel} = \sqrt{[v(1-a)]^2 + [\Omega r(1+a')]^2} \quad (22)$$

where a and a' are the axial velocity and tangential velocity induction factors.

The flow angle ϕ can be calculated by

$$\phi = \tan^{-1} \frac{v(1-a)}{\Omega r(1+a')} \quad (23)$$

The attack angle α between the relative velocity V_{rel} and and chord line is obtained as:

$$\alpha = \phi - \theta \quad (24)$$

where θ is the summation of the pitch angle and the twist which is predetermined by the airfoil.

In terms of the attack angle α , the lift and drag coefficients C_l and C_d can be determined from the airfoil data. The lift force P_L which is perpendicular and the drag force which is parallel to the relative velocity can be computed as:

$$P_L = \frac{1}{2}\rho V_{rel}^2 c C_l, \quad P_D = \frac{1}{2}\rho V_{rel}^2 c C_d \quad (25)$$

where ρ is the density of air and c is the chord length.

The normal and the tangential coefficients C_N and C_T are defined as:

$$C_N = \cos\phi C_l + \sin\phi C_d, \quad C_T = \sin\phi C_l - \cos\phi C_d \quad (26)$$

The normal and tangential forces P_N and P_T can be calculated as:

$$P_N = \frac{1}{2}\rho V_{rel}^2 c C_N, \quad P_T = \frac{1}{2}\rho V_{rel}^2 c C_T \quad (27)$$

Eqs. (22) through (27) demonstrate the primary procedure to calculate the aerodynamic load. In real application, a and a' are unknown and need to be determined via iterations. Matlab code has been developed to calculate the time series of P_N and P_T in the present study based on the algorithm proposed in [23]. Prandtl's tip loss factor and Glauert correction are considered in the Matlab code. Next the Principle of Virtual Work is applied to calculate the generalized aerodynamic load.

Under P_N and P_T , the virtual work δW_{wl} done by external wind load is:

$$\delta W_{wl} = \sum_{j=1}^3 \left\{ \int_0^R P_{Tj}(r, t) [\phi_{1e} \delta q_j + \delta u_{nac}^{ss} \cos(\psi_j)] dr + \int_0^R P_{Nj}(r, t) [\phi_{1f} \delta q_{j+3} + \delta u_{nac}^{fa}] dr \right\} \quad (28)$$

where $P_{Tj}(r, t)$ and $P_{Nj}(r, t)$ denote the tangential and normal wind loading intensity per unit length on the j^{th} blade.

In terms of the principles of work and energy, the generalized force Q_j can be determined as:

$$Q_j = \frac{\partial(\delta W_{wl})}{\partial(\delta q_j)} \quad (29)$$

Substituting Eqn. (28) into Eqn. (29) yields the wind induced generalized forces:

$$\begin{aligned} Q_{j,wind} &= \int_0^R P_{Tj}(r, t) \phi_{1e} dr, \quad Q_{j+3,wind} = \int_0^R P_{Nj}(r, t) \phi_{1f} dr, \quad j = 1, 2, 3 \\ Q_{7,wind} &= \sum_{j=1}^3 \int_0^R P_{Nj}(r, t) dr, \quad Q_{8,wind} = \sum_{j=1}^3 \int_0^R P_{Tj}(r, t) dr \cos(\psi_j), \quad Q_{9,wind} = Q_{7,wind} \\ Q_{10,wind} &= h Q_{7,wind}, \quad Q_{11,wind} = Q_{8,wind}, \quad Q_{12,wind} = h Q_{8,wind} \end{aligned} \quad (30)$$

Based on Eq. (31), the aerodynamic loading corresponding to an average wind speed of $v_0 = 12m/s$ at the hub height and a turbulence intensity of $TI = 10\%$ is computed. The first 60 second data are illustrated in Fig. 8 and Fig. 9.

3.3. Wave Loading

Wave loading on circular cylindrical structural members of fixed offshore structures can be estimated using Morison's equation[24]. For the monopile offshore wind turbine, the horizontal force dF acting on a

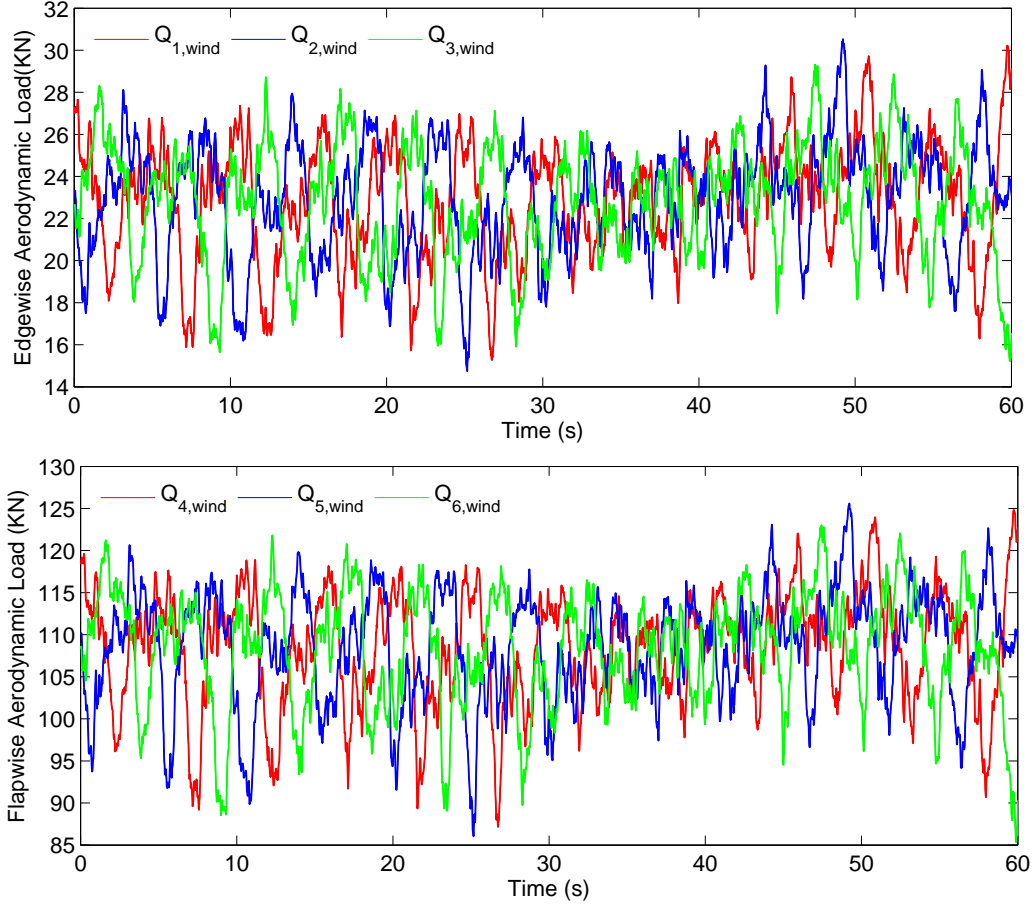


Figure 8: Aerodynamic loading applied on the blade. Upper: load in edgewise direction; lower: load in flapwise direction. Wind velocity at hub height is $v_0 = 12\text{m/s}$, turbulence intensity $TI = 10\%$.

strip of length dz (see Fig. 1) can be written as:

$$dF = \frac{\pi D^2}{4} C_M \rho \ddot{u} dz + \frac{\rho}{2} C_D D \dot{u} |\dot{u}| dz \quad (31)$$

where C_M and C_D are the mass and drag coefficients ($C_M = 1.0$ and $C_D = 1.2$ are adopted in the present paper); ρ is water density (1025kg/m^3), D is the diameter of the tower and the monopile; \ddot{u} and \dot{u} are the wave induced horizontal acceleration and velocity of fluid particles.

In terms of Ref. [28], JONSWAP spectrum as listed in Eq. (32) is used to generate wave time histories.

$$S(f) = 0.3125 H_s^2 T_p \left(\frac{f}{f_p} \right)^5 \exp \left[-\frac{5}{4} \left(\frac{f}{f_p} \right)^{-4} \right] (1 - 0.287 \ln \gamma) \gamma^{\exp \left[-\frac{(\omega - \omega_p)^2}{2\sigma^2 \omega_p^2} \right]} \quad (32)$$

where T_p is the wave period, H_s is the significant wave height, $f_p = 1/T_p$, $\sigma = 0.07$ for $f \leq f_p$, $\sigma = 0.09$ for $f > f_p$. Variable γ is the JONSWAP peakedness parameter [28]:

$$\gamma = \begin{cases} 5 & T_p / \sqrt{H_s} \leq 3.6 \\ \exp(5.75 - 1.15 T_p / \sqrt{H_s}) & 3.6 < T_p / \sqrt{H_s} \leq 5.0 \\ 1 & T_p / \sqrt{H_s} > 5.0 \end{cases} \quad (33)$$

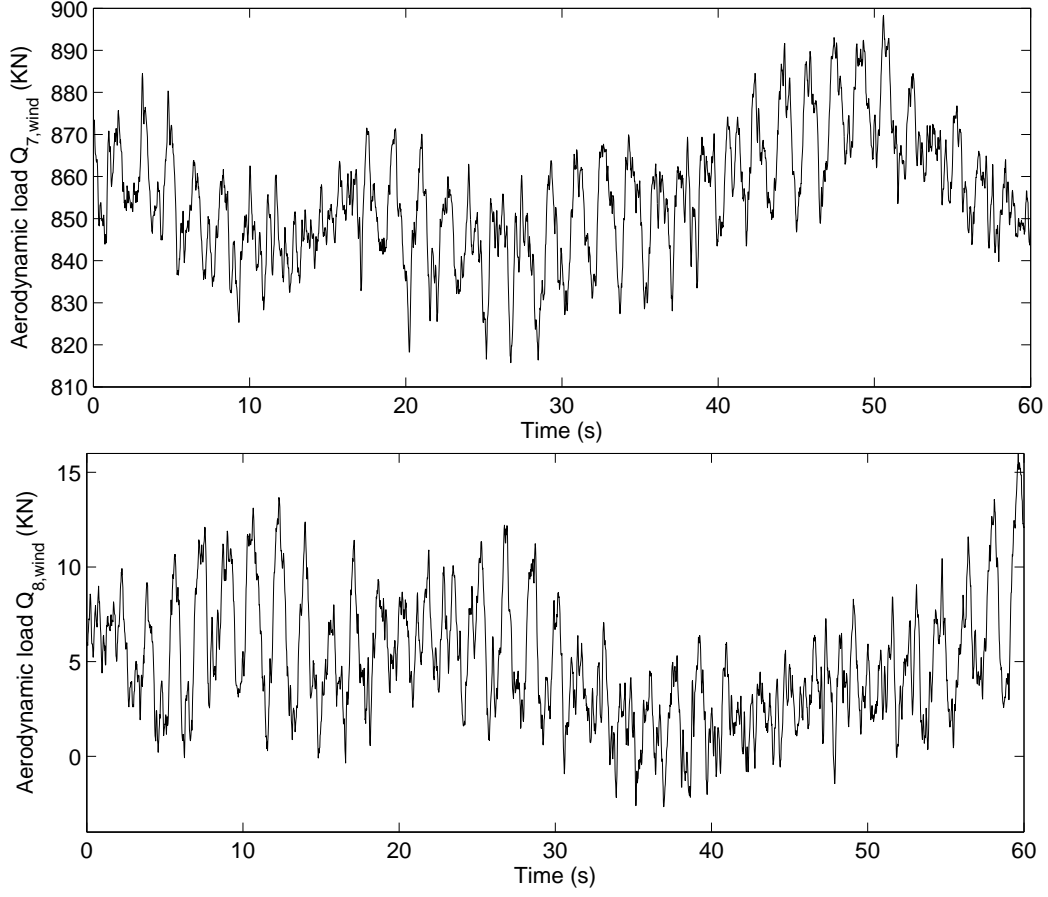


Figure 9: Aerodynamic loading applied on the nacelle. Upper: load in fore-aft direction; lower: load in side-side direction. Wind velocity at hub height is $v_0 = 12m/s$, turbulence intensity $TI = 10\%$.

Based on the spectrum representation method, the wave elevation $\eta(t)$, the fluid particle velocity u and the acceleration \dot{u} can be expressed as:

$$\eta(t) = \sum_{j=1}^N A_j \sin(\omega_j t - k_j x + \phi_j) \quad (34)$$

$$A_j = \sqrt{2S(\omega_j)\Delta\omega} \quad (35)$$

$$u = \sum_{j=1}^N \omega_j A_j \frac{\cosh[k(z + d_w)]}{T_w \sinh(kd_w)} \sin(\omega_j t - k_j x + \phi_j) \quad (36)$$

$$\dot{u} = \sum_{j=1}^N \omega_j^2 A_j \frac{\cosh[k(z + d_w)]}{T_w \sinh(kd_w)} \cos(\omega_j t - k_j x + \phi_j) \quad (37)$$

where k is wave number in m^{-1} , ω is wave frequency in rad/s , ϕ_j is a random phase angle uniformly distributed from 0 to 2π , d_w is the water depth, T_w is the wave period in s , z is the vertical ordinate from mean water level.

Given water depth z , the parameters ω and k are related by the dispersion equation [24]:

$$k \tanh kz = \omega^2/g \quad (38)$$

Hence, for any given water depth z , the wave number k can be determined via solving Eq. (38).

Virtual work δW_{wv} done by the wave load along virtual displacement δu_{tow} of the tower can be written as:

$$\delta W_{wv} = \int_0^\eta dF \delta u_{tow} = \int_0^\eta dF [\phi_{1t}(\cos\beta\delta q_7 + \sin\beta\delta q_8) + \cos\beta(\delta q_9 + z\delta q_{10}) + \sin\beta(\delta q_{11} + z\delta q_{12})] \quad (39)$$

where β is wind-wave misalignment angle.

Substituting Eq. (39) into into Eq. (29) yields the generalized forces corresponding to wave:

$$\begin{aligned} Q_{7,wave} &= \cos\beta F_{wv,1}, & Q_{8,wave} &= \sin\beta F_{wv,1} \\ Q_{9,wave} &= \cos\beta F_{wv,2}, & Q_{11,wave} &= \sin\beta F_{wv,2} \\ Q_{10,wave} &= \cos\beta F_{wv,3}, & Q_{12,wave} &= \sin\beta F_{wv,3} \end{aligned} \quad (40)$$

where

$$\begin{aligned} F_{wv,1} &= \int_{-d_w}^{\eta(t)} \phi_{1t}(z) dF = \sum_{i=1}^{N_z} \phi_{1t}(z_i) \left[\frac{\rho\pi D^2(z_i)}{4} C_M \ddot{u}(z_i, t) \Delta z + \frac{\rho}{2} C_D D(z_i) \dot{u}(z_i, t) |\dot{u}(z_i, t)| \Delta z \right] \\ F_{wv,2} &= \int_{-d_w}^{\eta(t)} dF = \sum_{i=1}^{N_z} \left[\frac{\rho\pi D^2(z_i)}{4} C_M \ddot{u}(z_i, t) \Delta z + \frac{\rho}{2} C_D D(z_i) \dot{u}(z_i, t) |\dot{u}(z_i, t)| \Delta z \right] \\ F_{wv,3} &= \int_{-d_w}^{\eta(t)} z dF = \sum_{i=1}^{N_z} \left[\frac{\rho\pi D^2(z_i)}{4} C_M \ddot{u}(z_i, t) \Delta z + \frac{\rho}{2} C_D D(z_i) \dot{u}(z_i, t) |\dot{u}(z_i, t)| \Delta z \right] z_i \end{aligned}$$

Parameter N_z denotes the number of segments that the wetted portion of the tower is divided, Δz denotes the segment length.

3.4. Seismic load

Let \ddot{u}_{gx} and \ddot{u}_{gy} denote the seismic acceleration components in x and y directions. Consider an infinitesimal unit dr of the blade, the effective earthquake force components acting on dr in x and y directions are $-\bar{m}\ddot{u}_{gx}dr$ and $-\bar{m}\ddot{u}_{gy}dr$. The virtual work $\delta W_{seismic,bl}$ done by seismic loading on the blades can be written as:

$$\delta W_{seismic,bl} = \sum_{j=1}^3 \left[\int_0^R -\bar{m}\ddot{u}_{gx}(\phi_{1f}\delta q_{j+3} + \delta u_{nac}^{fa})dr + \int_0^R -\bar{m}\ddot{u}_{gy}(\phi_{1e}\delta q_j \cos\psi_j + \delta u_{nac}^{ss})dr \right] \quad (41)$$

Similarly, the virtual work done by seismic loading on the nacelle and the tower are:

$$\delta W_{seismic,nac} = -\ddot{u}_{gx} M_{nac} \delta u_{nac}^{fa} - \ddot{u}_{gy} M_{nac} \delta u_{nac}^{ss} \quad (42)$$

$$\delta W_{seismic,tow} = -\int_0^h \ddot{u}_{gx} \bar{M} (\delta q_7 \phi_{tow}^1 + \delta q_9 + \delta q_{10} l) dl - \int_0^h \ddot{u}_{gy} \bar{M} \delta q_8 \phi_{tow}^1 dl \quad (43)$$

where M_{nac} denotes the mass of the nacelle, \bar{M} denotes the mass density of the tower in unit of kg/m , ϕ_{tow}^1 denotes the first mode shape of the tower.

Therefore, the total virtual work done by seismic loading on the entire wind turbine system can be obtained as:

$$\delta W_{seismic} = \delta W_{seismic,bl} + \delta W_{seismic,nac} + \delta W_{seismic,tow} \quad (44)$$

Substituting Eq. (44) into Eq. (29) yields the earthquake induced generalized forces:

$$\begin{aligned} Q_{j,seismic} &= -m_{1e} \cos(\psi_j) \ddot{u}_{gy}, & Q_{j+3,seismic} &= -m_{1f} \ddot{u}_{gx}, & j &= 1, 2, 3 \\ Q_{7,seismic} &= -(3m_0 + M_{nac} + M_{1tow}) \ddot{u}_{gx}, & Q_{8,seismic} &= -(m_0 \cos(\psi_j) + M_{nac} + M_{1tow}) \ddot{u}_{gy} \\ Q_{9,seismic} &= -(3m_0 + M_{nac} + M_{0tow}) \ddot{u}_{gx}, & Q_{10,seismic} &= -(3hm_0 + hM_{nac} + M_{2tow}) \ddot{u}_{gx} \\ Q_{11,seismic} &= -(3m_0 + M_{nac} + M_{0tow}) \ddot{u}_{gy}, & Q_{12,seismic} &= -(3hm_0 + hM_{nac} + M_{2tow}) \ddot{u}_{gy} \end{aligned} \quad (45)$$

where

$$M_{0tow} = \int_0^h \bar{M} dl, \quad M_{1tow} = \int_0^h \bar{M} \phi_{tow}^1 dl, \quad M_{2tow} = \int_0^h \bar{M} l dl \quad (46)$$

4. Optimum design

The optimum design for the 3d-PTMD to minimize the nacelle displacement RMS is presented in this section.

4.1. Optimum frequency and damping ratio

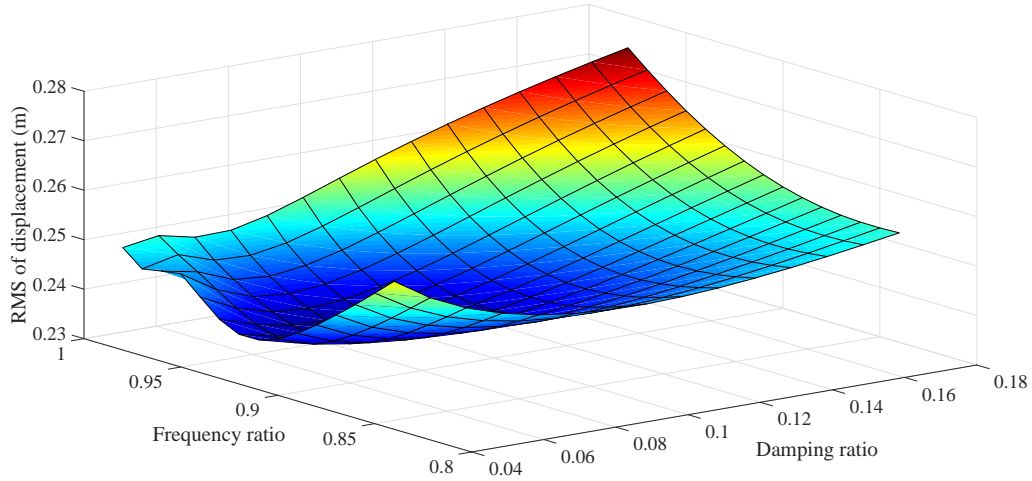


Figure 10: Displacement RMS under different frequency and damping ratio values.

A numerical search approach is utilized to obtain the optimum design. The displacement RMS is set as the optimum objective because load reduction, i.e., the displacement response mitigation, is the most important concern for wind turbines. With given mass ratio, the nacelle displacement RMS corresponding to different frequency and damping ratio values are calculated. Fig. 10 shows the nacelle displacement RMS against frequency and damping ratio where the mass ratio is 2%. In Fig. 10, the frequency and damping ratio that produces the minimum RMS is selected as the optimum design. A typical damping ratio value of 1% is adopted for the wind turbine tower during the numerical search. It is worthy to mention that different

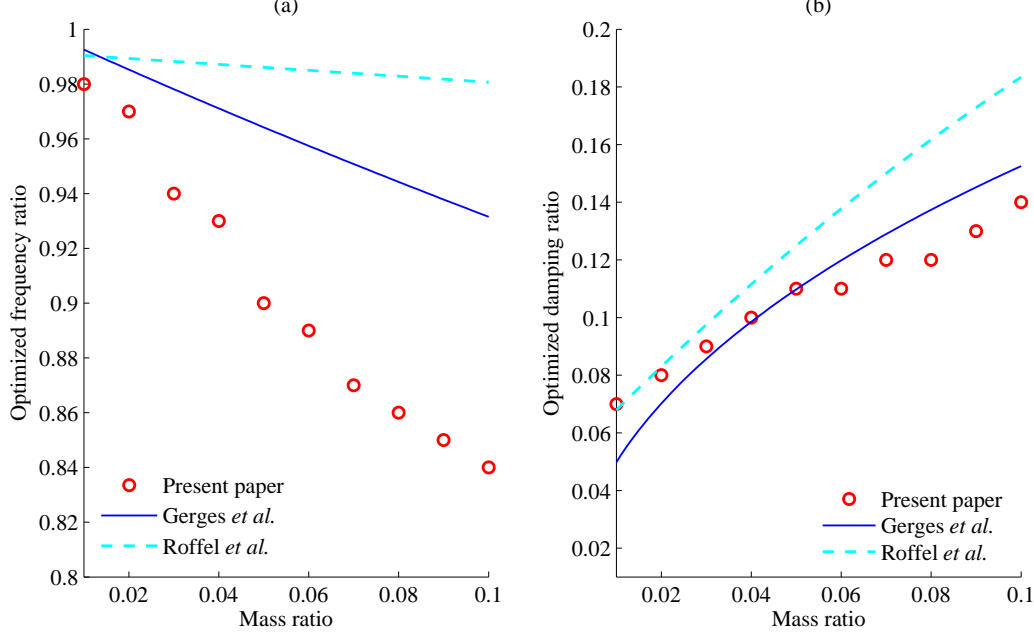


Figure 11: Optimum design of the 3d-PTMD.

wind-wave misalignment angles have been tested and little difference was observed. As a general case, a wind-wave misalignment angle of 30° is used when searching for the optimum design.

Fig. 11 (a) and (b) show the optimum frequency and damping ratio for the 3d-PTMD. The optimum design for the PTMD presented in Refs.[18, 19] are also illustrated in Fig. 11 for comparison. One can find in Fig. 11 (a) that the optimum frequency ratio obtained from the present study differs from the other two Refs. [18, 19]. The difference lies in the fact that Ref. [18] used a plane pendulum model and a zero damping ratio for the primary structure and Ref. [19] used the acceleration RMS as the optimization objective. Fig. 11 (b) shows that the difference of the optimum damping ratio from the present study is close to the result from Ref. [18] while smaller than the result from Ref. [19].

To facilitate engineering application, the optimum design formula is proposed as Eq. (47) through curve fitting with respect to the data presented in Fig. 11. Based on the optimum design formula, the effectiveness of the PTMD will be evaluated in the following section under combined wind, wave and seismic loading.

$$\begin{aligned} f_{opt} &= 7.6\mu^2 - 2.5\mu + 1 \\ \zeta_{opt} &= -2.7\mu^2 + \mu + 0.062 \end{aligned} \quad (47)$$

where μ is the mass ratio.

5. System Parameters

This section presents the associated parameter values of the baseline offshore wind turbine and the soil effects.

5.1. Model Parameters

The NREL 5 MW OC3 Mono-pile wind turbine model [26] is used in the present study. Details are presented in Table 1. The fundamental mode shapes(edgewise and flapwise) of the blade and the tower are formulated by Eq. (48) and illustrated in Fig. 12(a) and (b).

Table 1: Parameters of the NREL 5-MW baseline wind turbine[26]

Gross properties	Rating	5 MW
	Rotor diameter	126 m
	Hub height	90 m
	Cut-in, rated, cut-out wind speed	3 m/s, 11.4 m/s, 25 m/s
	Cut-in, rated rotor speed	6.9 rpm, 12.1 rpm
Blade	Length	61.5 m
	Mass	17,740 kg
	Second moment of inertia	11,776 kgm ²
	1 st edgewise mode natural frequency	1.08 Hz
	1 st flapwise mode natural frequency	0.68 Hz
	1 st mode damping ratio (edgewise and flapwise)	0.48%
Nacelle + hub	Nacelle mass	240,000 kg
	Hub mass	56,780 kg
	Hub diameter	3 m
Tower	Height above ground	87.6 m
	Overall (integrated) mass	267,650 kg
	1 st fore-aft mode natural frequency	0.324 Hz
	1 st side-side mode natural frequency	0.312 Hz
	1 st fore-aft(side-side) modal damping ratio	1%

$$\begin{aligned}
\phi_{1e}(\bar{r}) &= -0.6952\bar{r}^6 + 2.3760\bar{r}^5 - 3.5772\bar{r}^4 + 2.5337\bar{r}^3 + 0.3627\bar{r}^2 \\
\phi_{1f}(\bar{r}) &= -2.2555\bar{r}^6 + 4.7131\bar{r}^5 - 3.2452\bar{r}^4 + 1.7254\bar{r}^3 + 0.0622\bar{r}^2 \\
\phi_{1t}(\bar{h}) &= -0.6952\bar{h}^6 + 2.3760\bar{h}^5 - 3.5772\bar{h}^4 + 2.5337\bar{h}^3 + 0.3627\bar{h}^2
\end{aligned} \tag{48}$$

where $\bar{r} = r/61.5$ and $\bar{h} = h/87.6$ denote the normalized blade radius and tower height, separately.

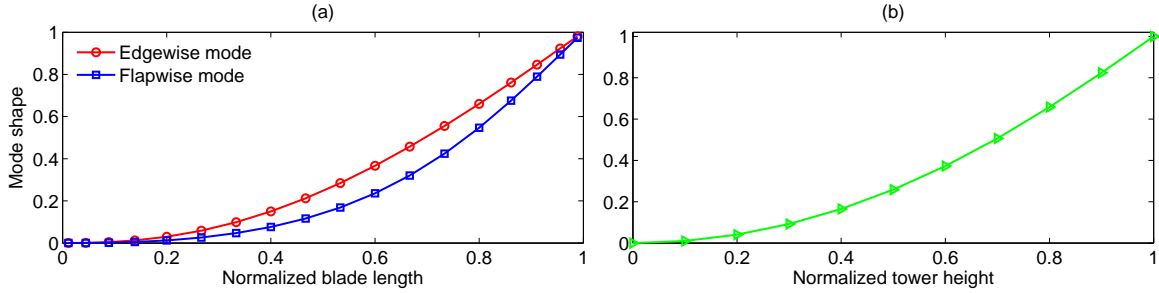


Figure 12: Fundamental mode shape of the blade and the tower. (a): mode shape of the blade (b): mode shape of the tower.

5.2. Soil effects parameters

Soil effect is considered via using linear springs and dash-pots as illustrated in Fig. 2. With reference to [27], value of parameters k_x , k_y , $k_{x\phi}$ and $k_{y\phi}$ are obtained as: $k_x = k_y = 3.89E9 \text{ N/m}$, $k_{x\phi} = k_{y\phi} = 1.14E11 \text{ Nm/rad}$ to represent clay soil condition. Soil damping properties c_x , c_y , $c_{x\phi}$ and $c_{y\phi}$ are selected such that the corresponding damping ratio are $\zeta_x = \zeta_y = \zeta_{x\phi} = \zeta_{y\phi} = 0.6\%$.

Table 2: Load cases considering wind, wave and seismic excitation

Load case 1(LC1)	Wind speed $v_0 = 12 \text{ m/s}$ at hub height $H = 90 \text{ m}$, Turbulence intensity $TI = 10\%$ Significant wave height $H_s = 3 \text{ m}$, Wave period $T_p = 10.0 \text{ s}$
Load case 2(LC2)	Wind turbine parked. 1994 Northridge NewHall fire station (NWH90, $M_w = 6.7$, $PGA = 0.59g$)
Load case 3(LC3)	Seismic loading + operational wind-wave loading LC1

6. Results

The effectiveness of the 3d-PTMD in controlling the bi-directional vibration of the offshore wind turbine is evaluated in this section.

6.1. Responses of uncontrolled wind turbine

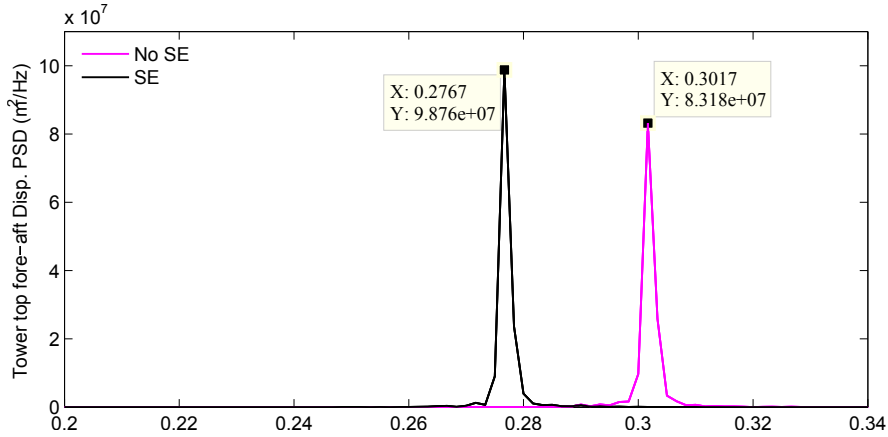


Figure 13: Response power spectrum with and without considering soil effect.

Fig. 13 illustrates the power spectrum of the wind turbine tower top response with and without considering soil effect. It is indicated in Fig. 13 that the structural natural frequency will be decreased by 8.3% when using the selected soil parameters representing clay soil condition.

6.2. Responses of controlled wind turbine under wind-wave misalignment

Structural responses of the wind turbine are computed through numerically solving Eq.(17). With reference to [28], a representative operational wind and wave loading as denoted as load case 1 in Table 2 is adopted. To simulate the wind turbines installed in the California coastal region, the recorded seismic acceleration of the Northridge earthquake Newhall 90 is utilized and denoted as load case 2. In Table 2, “LC” is the acronym for “load case”. Four representative wind-wave misalignment angles: 0° , 30° , 60° and 90° are used to evaluate the performance of the 3d-PTMD.

The dual TMDs model studied in Ref.[22] is adopted for comparison. In terms of Ref. [22], the optimal frequency and damping ratio are set as: $f_{opt} = 0.97$, $\zeta_{opt} = 8.2\%$ for mass ratio $\mu = 1\%$; $f_{opt} = 0.94$, $\zeta_{opt} = 11\%$ for mass ratio $\mu = 2\%$ and $f_{opt} = 0.9$, $\zeta_{opt} = 16\%$ for mass ratio $\mu = 4\%$.

Because the soil properties are in nature site-dependent and stochastic within a large area, it is difficult to collect sufficient data so as to exactly determine the natural frequency of the offshore wind turbines. In the present study, the original natural frequency of the wind turbine without considering the soil effects, i.e., $f_n = 0.3017 \text{ Hz}$ as shown in Fig. 13 is used when designing the dual TMDs and the 3d-PTMD.

Figs. 14 (a)-(d) show the bi-directional motion of the nacelle with and without the 3d-PTMD under the four misalignment angles. One can find in Fig. 14 (a) that the side-side displacement is minimal when wind

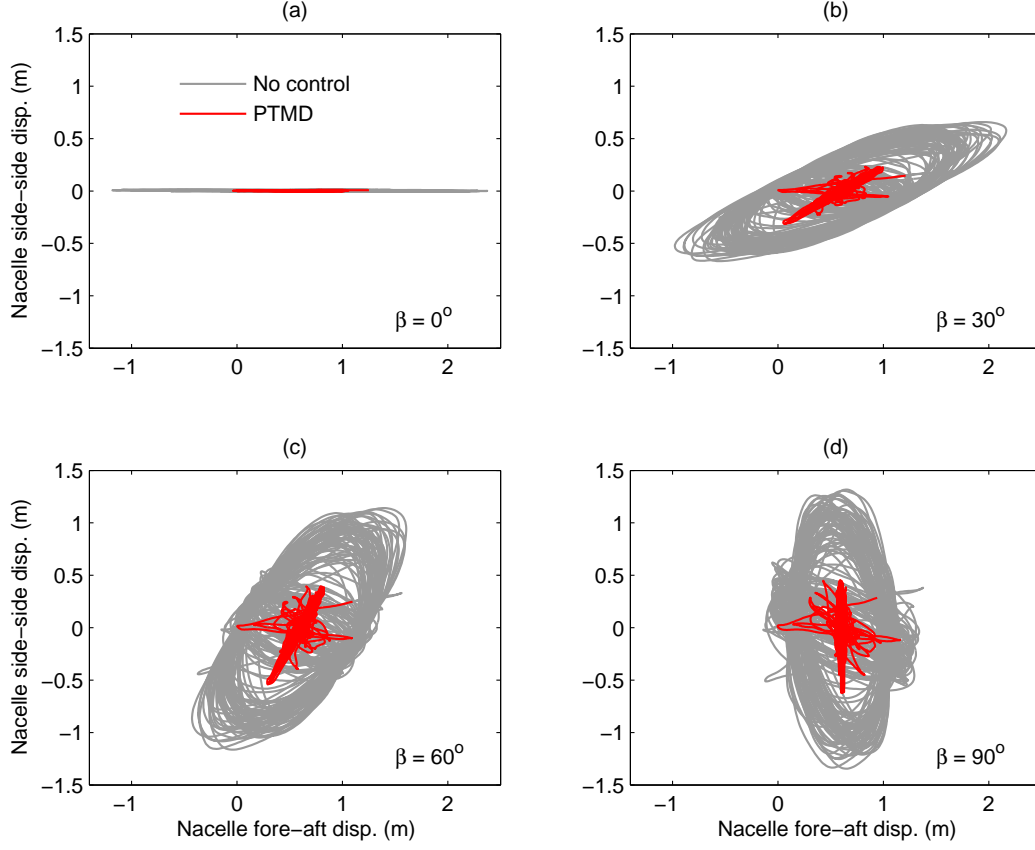


Figure 14: Nacelle response comparison with and without the 3d-PTMD under different wind-wave misalignment, mass ratio $\mu = 2\%$. (a): misalignment angle $\beta = 0^\circ$ (b): misalignment angle $\beta = 30^\circ$, (c): misalignment angle $\beta = 60^\circ$, (d): misalignment angle $\beta = 90^\circ$.

and wave loading are aligned. In comparison, the trajectory of the nacelle under a considerable wind-wave misalignment becomes more complex as shown in Fig. 14 (b)-(d). Through comparison, one can clearly observe that the motion of the nacelle can be significantly mitigated using the 3d-PTMD. Detailed reduction effect is listed in Table 3.

Figs. 15 (a)-(d) show the nacelle fore-aft displacement time-history comparison between the dual TMDs (referred to as “2TMD” hereafter) and the 3d-PTMD under the four wind-wave misalignment angles. It is found in Figs. 15(a)-(d) that the 3d-PTMD outperforms the 2TMD in mitigating the nacelle fore-aft response. In Fig. 15(a), the RMS response reduction can be improved by 12% using the PTMD. Detailed reduction comparison is illustrated in Table 3.

Figs. 16 (a)-(d) show the nacelle side-side displacement time-history comparison between the 2TMD and the 3d-PTMD. It is indicated in Fig. 16(a) that the side-side response is minimal when wind and wave are aligned. Figs. 16(b)-(d) indicate that the PTMD provides better reduction than the 2TMD. The side-side response increases as β increases. Quantitatively, in Fig. 16(b), the RMS response reduction is increased by 8% when using the 3d-PTMD. Fig. 17 shows the response spectrum of the data presented in Fig. 16(b). One can find that the response spectrum can be further mitigated by more than 50% when using the 3d-PTMD. More detailed response reduction is illustrated in Table 3.

Table 3 lists the RMS and peak response reduction with different mass ratios ranging from 2% to 5%. Through comparison, one can find that the 3d-PTMD outperforms the 2TMD in mitigating the RMS response (fore-aft and side-side) in that the former can improve the reduction effect by around 10%. It is also indicated

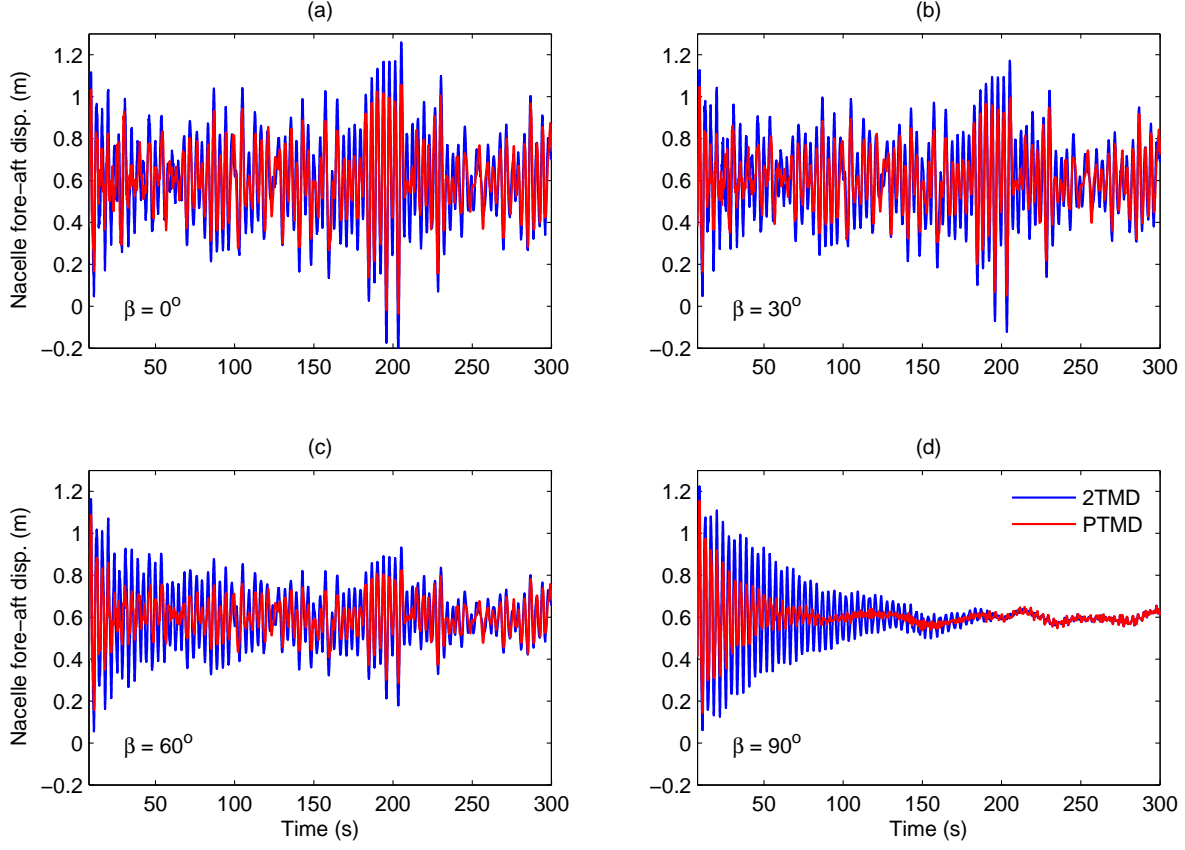


Figure 15: Nacelle fore-aft response mitigation comparison between the 3d-PTMD and the 2TMD under different wind-wave misalignment. (a): misalignment angle $\beta = 0^\circ$ (b): misalignment angle $\beta = 30^\circ$, (c): misalignment angle $\beta = 60^\circ$, (d): misalignment angle $\beta = 90^\circ$.

that as the mass ratio increases, the advantage of the PTMD over the 2TMD decreases and the marginal reduction effect of the 2TMD and the 3d-PTMD also decreases. Similar conclusions can be drawn with respect to the peak response reduction.

6.3. Responses under misaligned wind-wave and seismic loading

In comparison with wind and wave, seismic is relatively a rare event for wind turbines. Yet the combined effect of wind, wave and seismic loading, especially when considering the misalignment among the three, needs to be considered when evaluating the performance of the 3d-PTMD. In the present study, two scenarios, i.e., the parked condition(LC2) and the operational condition(LC3) are considered. The wind-wave misalignment angle is set to be $\beta = 30^\circ$. Different wind seismic misalignment angle β_2 have been used and similar results were obtained. As a general illustration, results corresponding to $\beta_2 = 90^\circ$ under load case LC3 are presented in Fig. 18 and Fig. 19. The seismic loading is set to start at $t = 150s$ and end at $t = 190s$.

Fig. 18(a) and (b) show the nacelle fore-aft and side-side displacement time-history comparison between the 2TMD and the 3d-PTMD under the operational condition LC3. It is indicated in Fig. 18(b) that when an earthquake occurs, the 3d-PTMD can mitigate the structural response to a lower level more quickly than the 2TMD.

Seismic loading with pulse-like characteristics will probably cause large acceleration which is detrimental to the nacelle with vulnerable mechanical devices. The reduction effect of the acceleration is presented in Fig. 19. Through comparing Fig. 19 (a) and (b), one can find that the seismic loading induced acceleration

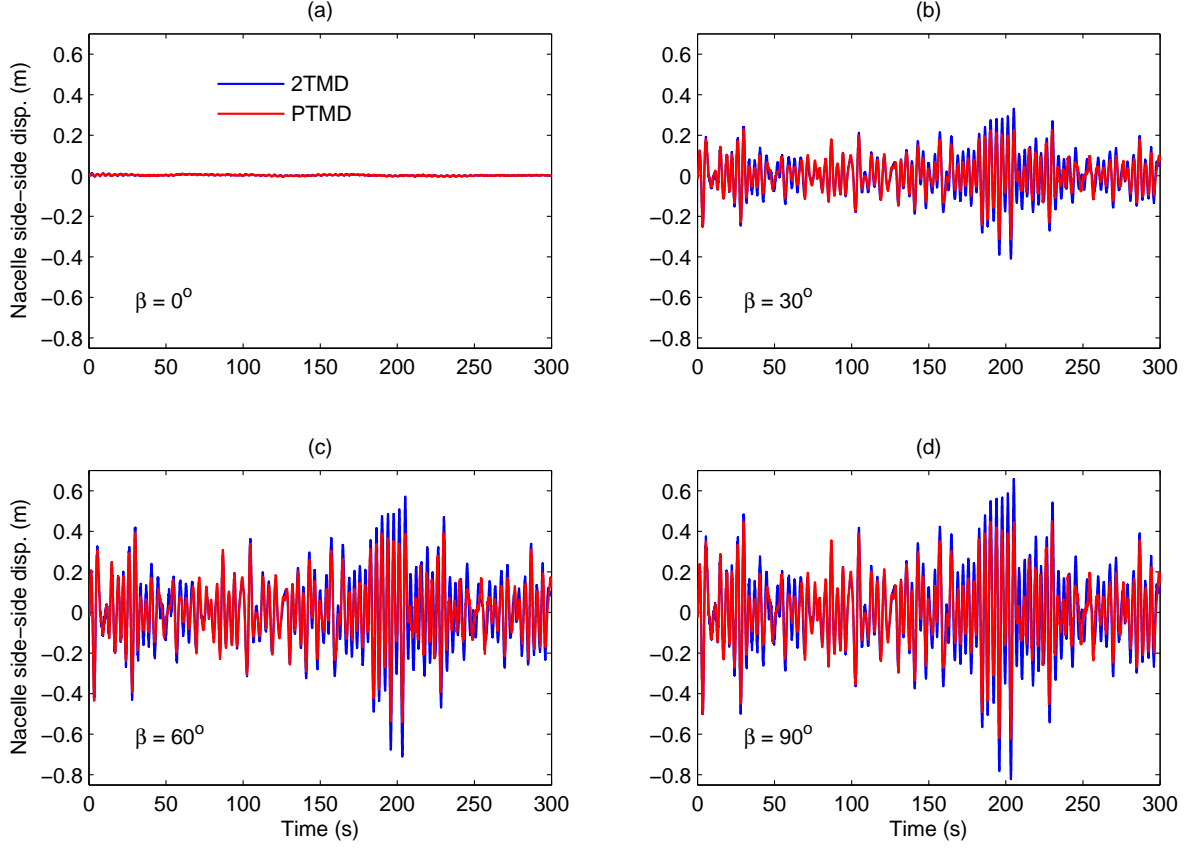


Figure 16: Nacelle side-side response mitigation comparison between the 3d-PTMD and the 2TMD under different wind-wave misalignment. (a): misalignment angle $\beta = 0^\circ$ (b): misalignment angle $\beta = 30^\circ$, (c): misalignment angle $\beta = 60^\circ$, (d): misalignment angle $\beta = 90^\circ$.

is roughly three times as large as that caused by operational wind and wave loading. In Fig. 19 (b), the mitigation of acceleration can be improved by around 50% by the 3d-PTMD when compared to the 2TMD.

TMD stroke is a critical index when evaluating the performance because of the limited space in the nacelle. Fig. 20 compares the stroke between the 2TMD and the 3d-PTMD under load case LC2 and LC3 and the selected misalignment angles. It can be observed that the 3d-PTMD has a much lower stroke than the 2TMD.

7. Conclusions

The present study proposes a 3d-PTMD to mitigate the bi-directional vibration of offshore wind turbines under misaligned wind-wave and seismic loading. The analytical model of the 3d-PTMD has been established and integrated with the analytical model of an offshore wind turbine established by the author. The optimum design formula of the 3d-PTMD has been determined via a numerical search approach and the performance is evaluated and compared with dual linear TMDs. Based on the results and discussions presented, the following four key conclusions can be obtained:

1. Because a nonlinear three dimensional pendulum model and a different optimum objective are utilized, the optimum design parameters obtained from the present study are different from the results presented in Refs.[18, 19]. The proposed design formula is focused on load reduction for offshore wind turbines

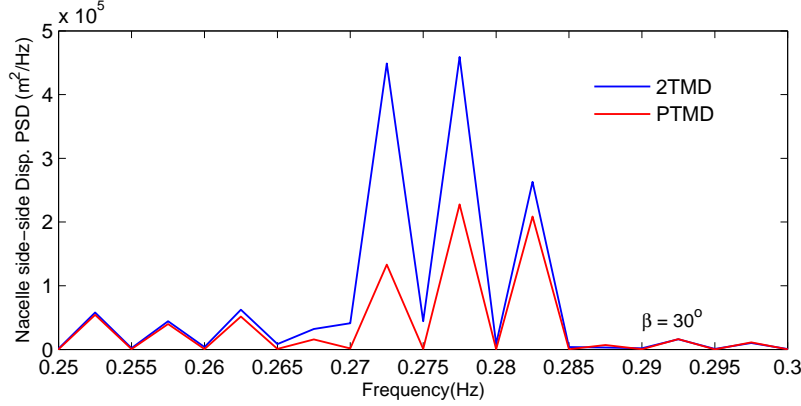


Figure 17: Nacelle fore-aft response spectrum comparison between the 3d-PTMD and the 2TMD under wind-wave misalignment angle $\beta = 30^\circ$.

Table 3: Response reduction comparison between the 2TMD and the 3d-PTMD under Load case LC1. Note: the first and second data of each pair correspond to the reduction of the 2TMD and the 3d-PTMD respectively.

β	$\mu = 2\%$		$\mu = 3\%$		$\mu = 4\%$		$\mu = 5\%$	
	FA	SS	FA	RMS response SS	FA	SS	FA	SS
0°	42%, 54%	26%, 34%	51%, 58%	30%, 37%	57%, 59%	33%, 37%	58%, 61%	34%, 38%
30°	45%, 58%	40%, 48%	53%, 61%	45%, 54%	60%, 62%	52%, 57%	60%, 62%	52%, 57%
60°	52%, 67%	40%, 49%	60%, 71%	45%, 54%	69%, 73%	52%, 57%	69%, 72%	52%, 57%
90°	60%, 74%	40%, 48%	65%, 80%	45%, 54%	77%, 84%	52%, 57%	77%, 84%	52%, 57%
β					Peak response			
	FA	SS	FA	SS	FA	SS	FA	SS
0°	20%, 24%	12%, 21%	24%, 30%	18%, 28%	27%, 34%	24%, 30%	28%, 37%	27%, 31%
30°	15%, 19%	17%, 34%	20%, 26%	29%, 45%	22%, 30%	37%, 48%	23%, 33%	40%, 54%
60°	6%, 11%	17%, 34%	11%, 19%	30%, 46%	14%, 23%	37%, 49%	16%, 27%	40%, 54%
90°	7%, 12%	17%, 34%	11%, 19%	30%, 46%	14%, 24%	37%, 49%	17%, 29%	40%, 54%

under misaligned wind and wave loading. Of course, the established model and the numerical search method can be used to obtain the optimum design suitable for other conditions.

2. When the 3d-PTMD is used, the bi-directional RMS and peak response of the nacelle under different misalignment angles can be mitigated remarkably under load case LC1, LC2 and LC3. In comparison, the reduction effect of the RMS response is better than that of the peak response since minimizing the RMS response is the optimum objective.
3. In comparison with the dual linear TMDs(2TMD), the 3d-PTMD can improve the reduction effect of the RMS response by around 12% and the peak response by an average value of 9% when mass ratio is 2%. As the mass ratio increases, the marginal RMS response reduction decreases for both the 2TMD and the 3d-PTMD. Therefore, a mass ratio value of $\mu = 2\% \sim 3\%$ is suggested for the 3d-PTMD considering reduction effect and practical application constraints.
4. Although a relatively rare event, seismic loading causes a much higher acceleration than the operational wind and wave loading. Application of the 3d-PTMD can mitigate the seismic induced acceleration more effectively than the 2TMD. In addition, the 3d-PTMD experiences smaller stroke than the 2TMD, which is beneficial to the nacelle from the perspective of practical application.

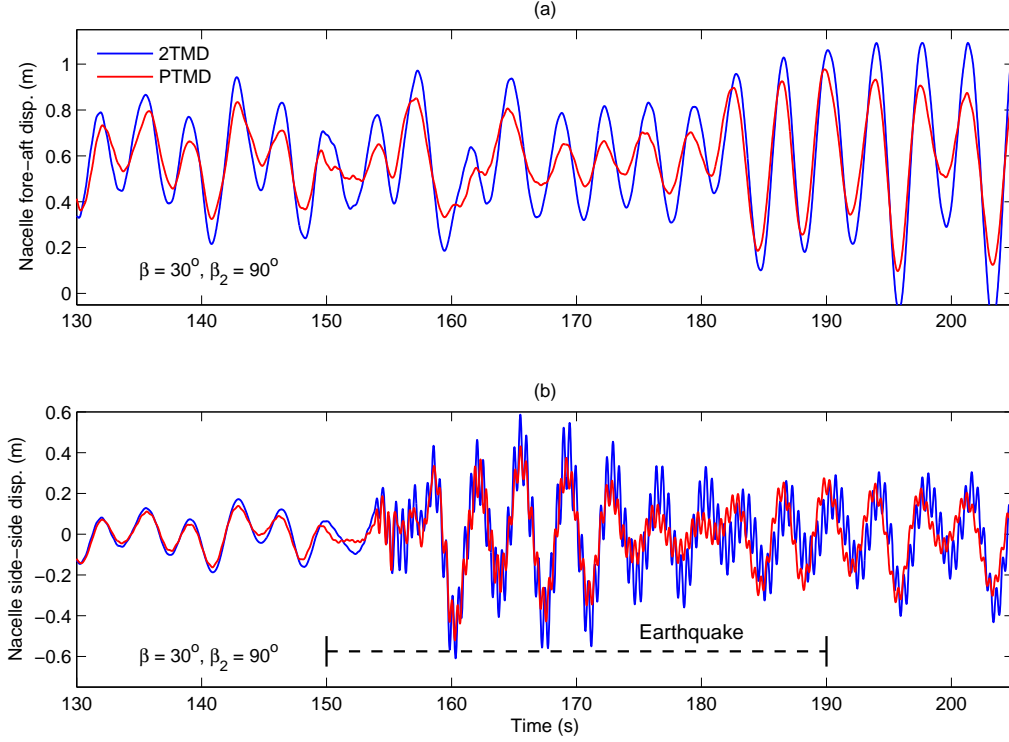


Figure 18: Nacelle displacement time-history comparison between the 2TMD and the PTMD under LC3.

Acknowledgment

This work was supported by Louisiana State University Start-up Fund (fund number is 127150013), the Faculty Research Grant (fund number is 127159132) and the Innovation in Engineering Research (FIRE) Grant provided by the College of Engineering at Louisiana State University. The author is grateful for all the support.

Appendix A

System matrices involved in Eqn. (17) for the uncontrolled 12-DOF system are:

$$\tilde{M} = \begin{bmatrix} m_1 & 0 & 0 & 0 & 0 & 0 & 0 & m_{18} & 0 & 0 & m_{18} & hm_{18} \\ 0 & m_1 & 0 & 0 & 0 & 0 & 0 & m_{28} & 0 & 0 & m_{28} & hm_{28} \\ 0 & 0 & m_1 & 0 & 0 & 0 & 0 & m_{38} & 0 & 0 & m_{38} & hm_{38} \\ 0 & 0 & 0 & m_2 & 0 & 0 & m_{47} & 0 & m_{47} & hm_{47} & 0 & 0 \\ 0 & 0 & 0 & 0 & m_2 & 0 & m_{47} & 0 & m_{47} & hm_{47} & 0 & 0 \\ 0 & 0 & 0 & 0 & 0 & m_2 & m_{47} & 0 & m_{47} & hm_{47} & 0 & 0 \\ 0 & 0 & 0 & m_{47} & m_{47} & m_{47} & m_7 & 0 & m_7 & hm_7 & 0 & 0 \\ m_{18} & m_{28} & m_{38} & 0 & 0 & 0 & 0 & m_8 & 0 & 0 & m_8 & hm_8 \\ 0 & 0 & 0 & m_{47} & m_{47} & m_{47} & m_7 & 0 & m_9 & hm_7 & 0 & 0 \\ 0 & 0 & 0 & hm_{47} & hm_{47} & hm_{47} & hm_7 & 0 & hm_7 & m_{10} & 0 & 0 \\ m_{18} & m_{28} & m_{38} & 0 & 0 & 0 & 0 & m_8 & 0 & 0 & m_{11} & hm_8 \\ hm_{18} & hm_{28} & hm_{38} & 0 & 0 & 0 & 0 & hm_8 & 0 & 0 & hm_8 & m_{12} \end{bmatrix} \quad (49)$$

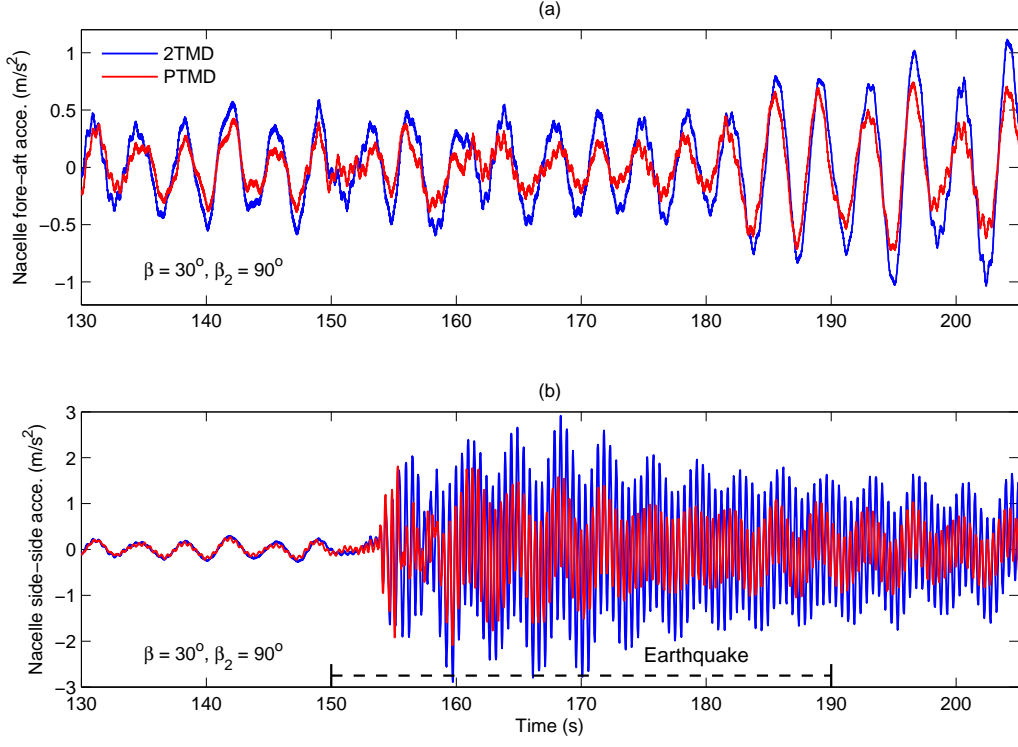


Figure 19: Nacelle acceleration time-history comparison between the 2TMD and the PTMD under LC3.

where

$$m_1 = \int_0^R \bar{m}(r) \phi_{1e}^2 dr, \quad m_2 = \int_0^R \bar{m}(r) \phi_{1f}^2 dr, \quad m_{j8} = \int_0^R \bar{m}(r) \phi_{1e} dr \cos \psi_j, \quad j = 1, 2, 3$$

$$m_{47} = \int_0^R \bar{m}(r) \phi_{1f} dr, \quad M_{1t} = \int_0^h \bar{M}(z) \phi_{1t}^2 dz, \quad m_8 = m_7 = 3m_0 + M_{nac} + M_{hub} + M_{1t}$$

$$m_9 = m_{11} = 3m_0 + M_{nac} + M_{hub} + M_t + M_f, \quad M_t = \int_0^h \bar{M}(z) dz, \quad m_{10} = m_{12} = I_f + h^2 m_7$$

Parameter m_0 denotes the mass of a single blade, M_{nac} and M_{hub} denote the mass of the nacelle and the hub, \bar{M} denotes the mass density (kg/m) of the tower, M_t denotes the mass of the tower, h_0 denotes the tower height, M_f and I_f denote the mass and moment of inertia of the foundation.

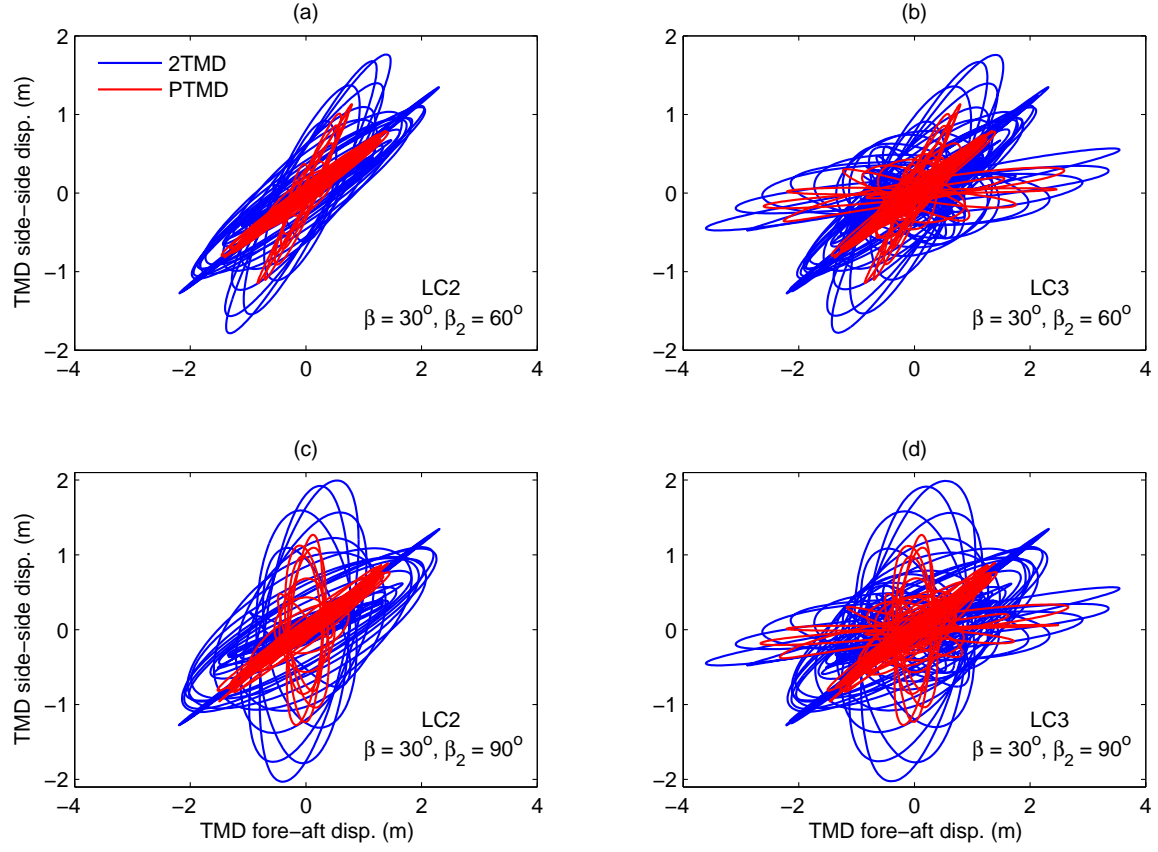


Figure 20: Stroke comparison between the 3d-PTMD and the 2TMD under different wind-wave misalignment. (a): misalignment angle $\beta = 0^\circ$ (b): misalignment angle $\beta = 30^\circ$, (c): misalignment angle $\beta = 60^\circ$, (d): misalignment angle $\beta = 90^\circ$.

$$\tilde{K} = \begin{bmatrix} k_{b1,eg} & 0 & 0 & 0 & 0 & 0 & 0 & 0 & 0 & 0 & 0 & 0 \\ 0 & k_{b2,eg} & 0 & 0 & 0 & 0 & 0 & 0 & 0 & 0 & 0 & 0 \\ 0 & 0 & k_{b3,eg} & 0 & 0 & 0 & 0 & 0 & 0 & 0 & 0 & 0 \\ 0 & 0 & 0 & k_{b1,fp} & 0 & 0 & 0 & 0 & 0 & 0 & 0 & 0 \\ 0 & 0 & 0 & 0 & k_{b2,fp} & 0 & 0 & 0 & 0 & 0 & 0 & 0 \\ 0 & 0 & 0 & 0 & 0 & k_{b3,fp} & 0 & 0 & 0 & 0 & 0 & 0 \\ 0 & 0 & 0 & 0 & 0 & 0 & k_7 & 0 & 0 & 0 & 0 & 0 \\ -\Omega^2 m_{18} & -\Omega^2 m_{28} & -\Omega^2 m_{38} & 0 & 0 & 0 & 0 & k_8 & 0 & 0 & 0 & 0 \\ 0 & 0 & 0 & 0 & 0 & 0 & 0 & 0 & k_x & 0 & 0 & 0 \\ 0 & 0 & 0 & 0 & 0 & 0 & 0 & 0 & 0 & k_{\phi x} & 0 & 0 \\ -\Omega^2 m_{18} & -\Omega^2 m_{28} & -\Omega^2 m_{38} & 0 & 0 & 0 & 0 & 0 & 0 & 0 & k_y & 0 \\ -h\Omega^2 m_{18} & -h\Omega^2 m_{28} & -h\Omega^2 m_{38} & 0 & 0 & 0 & 0 & 0 & 0 & 0 & 0 & k_{\phi y} \end{bmatrix} \quad (50)$$

where

$$k_{bj,eg} = k_{eg} + k_{ge,eg} - k_{gr,eg} \cos \psi_j - \Omega^2 m_1, \quad k_{bj,fp} = k_{fp} + k_{ge,fp} - k_{gr,fp} \cos \psi_j, \quad k_7 = k_8 = \int_0^h EI_t (\phi_{1t}'')^2 dz$$

$$\tilde{C} = \begin{bmatrix} c_{b,eg} & 0 & 0 & 0 & 0 & 0 & 0 & 0 & 0 & 0 & 0 & 0 \\ 0 & c_{b,eg} & 0 & 0 & 0 & 0 & 0 & 0 & 0 & 0 & 0 & 0 \\ 0 & 0 & c_{b,eg} & 0 & 0 & 0 & 0 & 0 & 0 & 0 & 0 & 0 \\ 0 & 0 & 0 & c_{b,fp} & 0 & 0 & 0 & 0 & 0 & 0 & 0 & 0 \\ 0 & 0 & 0 & 0 & c_{b,fp} & 0 & 0 & 0 & 0 & 0 & 0 & 0 \\ 0 & 0 & 0 & 0 & 0 & c_{b,fp} & 0 & 0 & 0 & 0 & 0 & 0 \\ 0 & 0 & 0 & 0 & 0 & 0 & c_7 & 0 & 0 & 0 & 0 & 0 \\ -2\Omega\bar{m}_{81} & -2\Omega\bar{m}_{82} & -2\Omega\bar{m}_{83} & 0 & 0 & 0 & 0 & c_8 & 0 & 0 & 0 & 0 \\ 0 & 0 & 0 & 0 & 0 & 0 & 0 & 0 & c_x & 0 & 0 & 0 \\ 0 & 0 & 0 & 0 & 0 & 0 & 0 & 0 & 0 & c_{\phi x} & 0 & 0 \\ -2\Omega\bar{m}_{81} & -2\Omega\bar{m}_{82} & -2\Omega\bar{m}_{83} & 0 & 0 & 0 & 0 & 0 & 0 & 0 & c_y & 0 \\ -2h\Omega\bar{m}_{81} & -2h\Omega\bar{m}_{82} & -2h\Omega\bar{m}_{83} & 0 & 0 & 0 & 0 & 0 & 0 & 0 & 0 & c_{\phi y} \end{bmatrix} \quad (51)$$

where

$$\bar{m}_{8j} = \int_0^R \bar{m}(r) \phi_{1e} dr \sin \psi_j, \quad j = 1, 2, 3$$

$c_{bj,eg}$ and $c_{bj,fp}$ denote the edgewise and flapwise structural and aerodynamic damping of the blade, c_7 and c_8 denote the damping in the fore-aft and side-side directions, including the structural and aerodynamic damping property of the nacelle and the tower, c_x and $c_{\phi x}$ denote the fore-aft translational and rotational damping of the foundation, c_y and $c_{\phi y}$ denote the side-side translational and rotational damping of the foundation.

Appendix B

System matrices involved in Eqn. (17) for the controlled 14-DOF system are:

$$\tilde{M} = \begin{bmatrix} m_1 & 0 & 0 & 0 & 0 & 0 & 0 & m_{18} & 0 & 0 & m_{18} & hm_{18} & 0 & 0 \\ 0 & m_1 & 0 & 0 & 0 & 0 & 0 & m_{28} & 0 & 0 & m_{28} & hm_{28} & 0 & 0 \\ 0 & 0 & m_1 & 0 & 0 & 0 & 0 & m_{38} & 0 & 0 & m_{38} & hm_{38} & 0 & 0 \\ 0 & 0 & 0 & m_2 & 0 & 0 & m_{47} & 0 & m_{47} & hm_{47} & 0 & 0 & 0 & 0 \\ 0 & 0 & 0 & 0 & m_2 & 0 & m_{47} & 0 & m_{47} & hm_{47} & 0 & 0 & 0 & 0 \\ 0 & 0 & 0 & 0 & 0 & m_2 & m_{47} & 0 & m_{47} & hm_{47} & 0 & 0 & 0 & 0 \\ 0 & 0 & 0 & m_{47} & m_{47} & m_{47} & M_7 & 0 & m_7 & hm_7 & 0 & 0 & m_p & 0 \\ m_{18} & m_{28} & m_{38} & 0 & 0 & 0 & 0 & M_8 & 0 & 0 & m_8 & hm_8 & 0 & m_p \\ 0 & 0 & 0 & m_{47} & m_{47} & m_{47} & m_7 & 0 & M_9 & hm_7 & 0 & 0 & m_p & 0 \\ 0 & 0 & 0 & hm_{47} & hm_{47} & hm_{47} & hm_7 & 0 & hm_7 & M_{10} & 0 & 0 & hm_p & 0 \\ m_{18} & m_{28} & m_{38} & 0 & 0 & 0 & 0 & m_8 & 0 & 0 & M_{11} & hm_8 & 0 & m_p \\ hm_{18} & hm_{28} & hm_{38} & 0 & 0 & 0 & 0 & hm_8 & 0 & 0 & hm_8 & M_{12} & 0 & hm_p \\ 0 & 0 & 0 & 0 & 0 & 0 & m_p & 0 & m_p & hm_p & 0 & 0 & D_1 m_p & D_{12} m_p \\ 0 & 0 & 0 & 0 & 0 & 0 & 0 & m_p & 0 & 0 & m_p & hm_p & D_{12} m_p & D_2 m_p \end{bmatrix} \quad (52)$$

where

$$M_7 = m_7 + m_p, \quad M_8 = m_8 + m_p, \quad M_9 = m_9 + m_p, \quad M_{11} = m_{11} + m_p, \quad M_{10} = m_{10} + h^2 m_p, \quad M_{12} = m_{12} + h^2 m_p,$$

$$D_1 = 1 + \frac{x_r^2}{z_r^2}, \quad D_{12} = \frac{x_r y_r}{z_r^2}, \quad D_2 = 1 + \frac{y_r^2}{z_r^2}$$

m_p denotes the mass of the pendulum

$$\tilde{K} = \begin{bmatrix} k_{b1,eg} & 0 & 0 & 0 & 0 & 0 & 0 & 0 & 0 & 0 & 0 & 0 & 0 & 0 \\ 0 & k_{b2,eg} & 0 & 0 & 0 & 0 & 0 & 0 & 0 & 0 & 0 & 0 & 0 & 0 \\ 0 & 0 & k_{b3,eg} & 0 & 0 & 0 & 0 & 0 & 0 & 0 & 0 & 0 & 0 & 0 \\ 0 & 0 & 0 & k_{b1,fp} & 0 & 0 & 0 & 0 & 0 & 0 & 0 & 0 & 0 & 0 \\ 0 & 0 & 0 & 0 & k_{b2,fp} & 0 & 0 & 0 & 0 & 0 & 0 & 0 & 0 & 0 \\ 0 & 0 & 0 & 0 & 0 & k_{b3,fp} & 0 & 0 & 0 & 0 & 0 & 0 & 0 & 0 \\ 0 & 0 & 0 & 0 & 0 & 0 & k_7 & 0 & 0 & 0 & 0 & 0 & 0 & 0 \\ -\Omega^2 m_{18} & -\Omega^2 m_{28} & -\Omega^2 m_{38} & 0 & 0 & 0 & 0 & k_8 & 0 & 0 & 0 & 0 & 0 & 0 \\ 0 & 0 & 0 & 0 & 0 & 0 & 0 & 0 & k_x & 0 & 0 & 0 & 0 & 0 \\ 0 & 0 & 0 & 0 & 0 & 0 & 0 & 0 & 0 & k_{\phi x} & 0 & 0 & 0 & 0 \\ -\Omega^2 m_{18} & -\Omega^2 m_{28} & -\Omega^2 m_{38} & 0 & 0 & 0 & 0 & 0 & 0 & 0 & k_y & 0 & 0 & 0 \\ -h\Omega^2 m_{18} & -h\Omega^2 m_{28} & -h\Omega^2 m_{38} & 0 & 0 & 0 & 0 & 0 & 0 & 0 & 0 & k_{\phi y} & 0 & 0 \\ 0 & 0 & 0 & 0 & 0 & 0 & 0 & 0 & 0 & 0 & 0 & 0 & m_p g / z_r & 0 \\ 0 & 0 & 0 & 0 & 0 & 0 & 0 & 0 & 0 & 0 & 0 & 0 & 0 & m_p g / z_r \end{bmatrix} \quad (53)$$

$$\tilde{C} = \begin{bmatrix} c_{b,eg} & 0 & 0 & 0 & 0 & 0 & 0 & 0 & 0 & 0 & 0 & 0 & 0 & 0 \\ 0 & c_{b,eg} & 0 & 0 & 0 & 0 & 0 & 0 & 0 & 0 & 0 & 0 & 0 & 0 \\ 0 & 0 & c_{b,eg} & 0 & 0 & 0 & 0 & 0 & 0 & 0 & 0 & 0 & 0 & 0 \\ 0 & 0 & 0 & c_{b,fp} & 0 & 0 & 0 & 0 & 0 & 0 & 0 & 0 & 0 & 0 \\ 0 & 0 & 0 & 0 & c_{b,fp} & 0 & 0 & 0 & 0 & 0 & 0 & 0 & 0 & 0 \\ 0 & 0 & 0 & 0 & 0 & c_{b,fp} & 0 & 0 & 0 & 0 & 0 & 0 & 0 & 0 \\ 0 & 0 & 0 & 0 & 0 & 0 & c_7 & 0 & 0 & 0 & 0 & 0 & -c_{px} & 0 \\ -2\Omega \bar{m}_{81} & -2\Omega \bar{m}_{82} & -2\Omega \bar{m}_{83} & 0 & 0 & 0 & 0 & c_8 & 0 & 0 & 0 & 0 & 0 & -c_{py} \\ 0 & 0 & 0 & 0 & 0 & 0 & 0 & 0 & c_x & 0 & 0 & 0 & 0 & 0 \\ 0 & 0 & 0 & 0 & 0 & 0 & 0 & 0 & 0 & c_{\phi x} & 0 & 0 & 0 & 0 \\ -2\Omega \bar{m}_{81} & -2\Omega \bar{m}_{82} & -2\Omega \bar{m}_{83} & 0 & 0 & 0 & 0 & 0 & 0 & 0 & c_y & 0 & 0 & 0 \\ -2h\Omega \bar{m}_{81} & -2h\Omega \bar{m}_{82} & -2h\Omega \bar{m}_{83} & 0 & 0 & 0 & 0 & 0 & 0 & 0 & 0 & c_{\phi y} & 0 & 0 \\ 0 & 0 & 0 & 0 & 0 & 0 & 0 & 0 & 0 & 0 & 0 & 0 & c_{px} & 0 \\ 0 & 0 & 0 & 0 & 0 & 0 & 0 & 0 & 0 & 0 & 0 & 0 & 0 & c_{py} \end{bmatrix} \quad (54)$$

where c_{px} and c_{py} are the viscous damping coefficients of the pendulum damper in the fore-aft and side-side directions.

$$\tilde{F} = \{ 0 \ 0 \ 0 \ 0 \ 0 \ 0 \ 0 \ 0 \ 0 \ 0 \ 0 \ 0 \ 0 \ f_{13} \ f_{14} \}^T \quad (55)$$

where

$$\begin{aligned} f_{13} &= -\frac{x_r}{z_r^4} (x_r \dot{x}_r + y_r \dot{y}_r)^2 - \frac{x_r}{z_r^2} (\dot{x}_r^2 + \dot{y}_r^2) \\ f_{14} &= -\frac{y_r}{z_r^4} (x_r \dot{x}_r + y_r \dot{y}_r)^2 - \frac{y_r}{z_r^2} (\dot{x}_r^2 + \dot{y}_r^2) \end{aligned}$$

References

- [1] G. Housner, L.A. Bergman, T.K. Caughey, A.G. Chassiakos etc., Structural control: past, present, and future, Journal of Engineering Mechanics. 123(9) (1997) 897–971.
- [2] B. Spencer, S. Nagarajaiah, State of the art of structural control, Journal of Structural Engineering. 129(7) (2003) 845–856.

- [3] P. Murtagh, A. Ghosh, B. Basu, B. Broderick, Passive control of wind turbine vibrations including blade/tower interaction and rotationally sampled turbulence, *Wind Energy*. 11 (2007) 305–317.
- [4] S. Colwell, B. Basu, Tuned liquid column dampers in offshore wind turbines for structural control, *Engineering Structures*. 31 (2009) 358–368.
- [5] M. Lackner, M. Rotea, Passive structural control of offshore wind turbines, *Wind Energy*. 14 (2011) 373–388.
- [6] S. Nagarajaiah, E. Sonmez, Structures with semiactive variable stiffness single/multiple tuned mass dampers, *Journal of Structural Engineering*. 133(1) (2007) 67–77.
- [7] S. Nagarajaiah, Adaptive passive, semiactive, smart tuned mass dampers: identification and control using empirical mode decomposition, hilbert transform, and short-term fourier transform, *Structural Control and Health Monitoring*. 16(7-8) (2009) 800–841.
- [8] C. Sun, S. Nagarajaiah, A. Dick, Experimental Investigation of Vibration Attenuation Using Nonlinear Tuned Mass Damper and Pendulum Tuned Mass Damper in Parallel, *Nonlinear Dynamics*. 78(4) (2014) 2699–2715.
- [9] F. Weber, Semi-active vibration vibration absorber based on real-time controlled MR damper, *Mechanical System and Signal Processing*. 46(2014) 272–288.
- [10] C. Huang, J. Arrigan, S. Nagarajaiah, B. Basu, Semi-Active Algorithm for Edgewise Vibration Control in Floating Wind Turbine Blades. Conference: 12th Biennial International Conference on Engineering, Construction, and Operations in Challenging Environments, p. 2097–2110, 2010.
- [11] J. Arrigan, V. Pakrashi, B. Basu, S. Nagarajaiah, Control of flapwise vibrations in wind turbine blades using semi-active tuned mass dampers, *Struct. Control Health Monit.* 18(2011) 840–851.
- [12] C. Sun, S. Nagarajaiah, Study on Semi-active Tuned Mass Damper with Variable Damping and Stiffness under Seismic Excitations, *Structural Control and Health Monitoring*. 21(6) (2014) 890–906.
- [13] C. Sun, Semi-active control of monopile offshore wind turbines under multi-hazards. *Mechanical Systems and Signal Processing*. 99(15) (2018) 285–305.
- [14] V. Gupta, M. Sharma, N. Thakur, Active structural vibration control: Robust to temperature variations, *Mechanical System and Signal Processing* 33 (2012) 167–180.
- [15] C. Dogruer , A. Pirsoltan, Active vibration control of a single-stage spur gearbox, *Mechanical System and Signal Processing* 85 (2017) 429–444.
- [16] A. Staino, B. Basu, S. Nielsen, Actuator control of edgewise vibrations in wind turbine blades, *J. Sound Vib.* 331 (2012) 1233–1256.
- [17] B. Fitzgerald, B. Basu, Cable connected active tuned mass dampers for control of in-plane, *J. Sound Vib.* 333 (2014) 5980–6004.
- [18] R. Gerges, B. Vickery, Optimum design of pendulum type tuned mass dampers. *Struct. Design Tall Spec. Build.* 14(4) (2005) 353–368.
- [19] A. Roffel, S. Narasimhan, T. Haskett, Performance of Pendulum Tuned Mass Dampers in Reducing the Responses of Flexible Structures. *Journal of Structural Engineering* 139(12) (2013) 04013019.
- [20] B.J. Jonkman, L. Kilcher, TurbSim User’s Guide: Version 1.06.00 *National Renewable Energy Laboratory* 2012; Technical Report.

- [21] C. Sun, S. Nagarajaiah, A. Dick, Family of smart tuned mass dampers with variable frequency under harmonic excitations and ground motions: closed-form evaluation. *Smart Structures and Systems* 13(2) (2014) 319–341.
- [22] G. Stewart, M. Lackner, Offshore Wind Turbine Load Reduction Employing Optimal Passive Tuned Mass Damping Systems. *IEEE TRANSACTIONS ON CONTROL SYSTEMS TECHNOLOGY* 21(4) (2013) 1090–1104.
- [23] Hansen MOL. Aerodynamics of wind turbines. *James & James (Science Publishers) Ltd* 2000.
- [24] Faltinsen OM. *Sea Loads on Ships and Offshore Structures*. Cambridge University Press: Cambridge, UK, 1990.
- [25] Cohen L. *Time-frequency analysis: theory and applications*. Prentice Hall, 1995.
- [26] Jonkman J., Butterfield S., Musial W., Scott G. *Definition of a 5-MW Reference Wind Turbine for Offshore Systems Development*. Technical Report, NREL 2009.
- [27] Carswell W., Johansson J., Lovholt F., Arwade S.R., Madshus C., DeGroot D.J., Myers A.T., Foundation damping and the dynamics of offshore wind turbine monopiles. *Renewable Energy* 80 (2015) 724–736.
- [28] IEC. *Wind turbines. Part 3: design requirements for offshore wind turbines*. IEC 61400-3 (ed. 1) 2009, Geneva, Switzerland: International Electrotechnical Commission.